ISSN 1849–0751 (On–line)
ISSN 0013–7448 (Print)
UDK 621.31
https://doi.org/10.37798/
EN2026751

Journal of Energy

VOLUME 75 Number 1 | 2026

ENERGIJA 75

03 Mario Matijević, Matej Pekeč
Hybrid Shielding Calculations of GBC32 Cask

09 Davor Grgić, Nikola Novosel, Paulina Družijanić, Petra Strmečki
Natural Heat Transfer Performance of Helium Filled Spent Fuel Multi Purpose Container Calculated for Different Initial Pressures

18 Petar Vinković, Renata Rubeša, Goran Levačić
Development and Validation of Dynamic RMS Models for Power System Analysis

24 Muhammad Rashid, Syed Mohammad Ali Shah, Abdur Raheem, Saeed Uddin Shaikh, Rabia Shakoor, Zeeshan Ahmad Arfee
Smart Hybrid Metaheuristic Model for Enhanced Wind Energy Production

Journal of Energy

Scientific Professional Journal Of Energy, Electricity, Power Systems
Online ISSN 1849–0751, Print ISSN 0013–7448, VOL 74
https://doi.org/10.37798/EN2024744

Published by
HEP d.d., Ulica grada Vukovara 37, HR–10000 Zagreb
HRO CIGRÉ, Berislavićeva 6, HR–10000 Zagreb
University of Zagreb FER, Unska 3, HR–10000 Zagreb

EDITORIAL

First paper of this issue, titled „Hybrid Shielding Calculations of GBC32 Cask“ evaluates the radiation shielding performance of the Generic Burnup Credit Cask (GBC-32) containing 32 Westinghouse 17x17 spent fuel assemblies using hybrid Monte Carlo methods. The authors employ the MAVRIC sequence in SCALE6.1.3 with FW-CADIS variance reduction to quantify neutron-gamma radiation fields and dose rates. A specialized C-language routine was developed to process ORIGEN-ARP multigroup data and generate normalized neutron-gamma spectra. Three fuel loading patterns were investigated, ranging from generic single-zone to realistic three-zone configurations. Results demonstrate compliance with regulatory dose rate limits under normal conditions (200 mrem/h at surfaces, 10 mrem/h at 2 m distance), while accidental scenarios without neutron shielding were also analyzed. The successful application of advanced variance reduction techniques achieved global flux convergence in both radial and axial directions.

Grgić et al. in their computationl study presented in second article „Natural Heat Transfer Performance of Helium Filled Spent Fuel Multi Purpose Container Calculated for Different Initial Pressures“ investigate the thermal performance of Holtec's Multi Purpose Container (MPC) for 37 spent fuel assemblies under varying helium fill pressures using Ansys Fluent. The authors developed a simplified model to analyze natural circulation heat transfer for the limiting heat load from NPP Krško SFDS Campaign 1 (22.17 kW). Simulations were performed at reference (4 bar), intermediate (6 bar), and limiting (8 bar) pressures. Key findings include maximum fuel temperatures decreasing from 404 K at 4 bar to 386 K at 8 bar, while MPC surface temperatures showed smaller reductions (374 K to 371 K). The study compared explicit fuel assembly geometry versus equivalent porous media models, demonstrating that the simplified approach provides adequate accuracy with significantly reduced computational cost. Importantly, the authors established a relationship between helium top-to-bottom temperature differential and pressure decrease, which can serve as an indicator of cask leakage. The influence of aluminum support inserts, concrete base, and non-uniform power distribution was systematically evaluated.

In the paper „Development and Validation of Dynamic RMS Models for Power System Analysis“ a comprehensive validation procedure for root-mean-square (RMS) dynamic models of synchronous generators, applied to Unit D of the Zakučac hydropower plant in Croatia is presented. Using high-resolution phasor measurement unit (PMU) data from a real system disturbance, the authors demonstrate systematic parameter tuning and model validation. The validation process included data preparation, static model alignment with steady-state measurements, and detailed tuning of inertia, time constants, reactances, and excitation system parameters. Initial simulations revealed discrepancies that were resolved through systematic parameter adjustment and incorporation of a reactive power (Q-regulator) supervisory control. The final validated model showed excellent agreement between measured and simulated active and reactive power responses, particularly during the critical first seconds following disturbance. The paper emphasizes the growing importance of accurate dynamic models as renewable energy integration reduces system inertia and increases vulnerability to transients.

Final paper in this issue presents a hybrid Particle Swarm Optimization-Genetic Algorithm (PSO-GA) approach for wind farm layout optimization (WFLO) aimed at maximizing energy extraction while minimizing wake losses. The proposed three-phase strategy was applied to realistic wind farm scenarios with varying wake conditions. Using the Jensen wake model for computational efficiency, the hybrid approach achieved consistent 20-28% reduction in wake losses compared to standalone PSO-based methods, with only 10-15% increase in computational time (approximately 20 seconds per simulation). Three case studies demonstrated the robustness of the method under different wind conditions, with 0.2% efficiency gain per case compared to benchmark approaches. The hybrid PSO-GA successfully identifies optimal turbine placement while maintaining industry-standard spacing constraints to prevent severe wake interference.

Igor Kuzle
Editor–in–Chief

Scientific paper
Manuscript received November 20, 2025; revised December 5, 2025; accepted January 14, 2026

Journal of Energy

VOLUME 75 Number 1 | 2026

journal homepage: http://journalofenergy.com/

Hybrid Shielding Calculations of GBC32 Cask

Mario Matijević, Matej Pekeč

***Summary* — This paper presents an evaluation of the shielding performance of the Generic Burnup Credit Cask (GBC-32) containing 32 Westinghouse 17x17 spent fuel assemblies. The spent fuel source term characterization was done in previous work, for which burnup/depletion calculations of TRITON-NEWT in tandem with ORIGEN-S were performed, generating collapsed cross section libraries as a function of fuel enrichment and burnup level. The hybrid shielding methodology of MAVRIC sequence in SCALE6.1.3 code was used to quantify neutron-gamma radiation field and dose rates around the cask, taking previously prepared source terms with ORIGEN-ARP module. For that purpose, to expedite the input preparation, a special routine in C-language was programmed to read ORIGEN-ARP multigroup output data and provide normalized neutron-gamma (n-g) spectra with the associated intensities (particles/s/MTU). This distributed multisource in Monte Carlo cask model included spent fuel neutrons and photons, photons from (n,g) reactions and photons from activated upper/lower hardware regions of spent fuel assemblies. Different fuel loading patterns were investigated, ranging from generic (one zone) to more realistic one (three zones) using averaged values of burnup, fuel enrichment and cooling time period. The FW-CADIS variance reduction technique was successfully applied for achieving global neutron-gamma flux convergence in radial and axial directions of the cask. The presented MC dosimetry results correspond to normal cask conditions, but an accidental scenario was also investigated, for which the resin neutron shield was removed from the shielding configuration.**

***Keywords* — SCALE6.1.3, FW-CADIS, cask, shielding, dose rates**

I. Introduction

The GBC-32 cask is an artificial model that combines the information from several actual cask submittals in the shielding safety analysis report (SARP). It was developed for the purpose of burnup-credit criticality studies with all the attributes of a realistic storage or transportation cask [1]. The shielding study of the GBC-32 cask was performed in this paper to evaluate compliance with dose rate limits of 10CFR71.47 for normal conditions and 10CFR71.51 for accidental conditions [2]. These regulatory limits are 200 mrem/h on the cask top and bottom surface, and 10 mrem/h at the 2 m location away from the cask. For accidental conditions this regulatory limit is increased to 1000 mrem/h.

(Corresponding author: Mario Matijević)

Mario Matijević and Matej Pekeč are with the University of Zagreb Faculty of Electrical Engineering and Computing, Zagreb, Croatia (email: mario.matijevic@fer.hr, matej.pekec@fer.hr)

The cask body is basically consisting of inner shell (stainless steel) and outer shell (resin) with a top and bottom lid providing shielding in axial direction. To provide a conservative approach, the impact limiters (wood inside steel casing) and boral panels between fuel assemblies (FAs) were omitted from the model. The spent fuel source terms used in this study were previously prepared with ORIGEN-ARP module [3], based on calculation framework of the TRITON-NEWT in tandem with ORIGEN-S module [4], generating collapsed cross section libraries from 238 to 49 neutron groups as a function of fuel enrichment and burnup level [5]. The fuel assembly is optimized Westinghouse 17x17 (OFA), with specific dimensions and materials taken from the reference [1]. From the shielding perspective, one arrives at distributed multisource in Monte Carlo (MC) cask model, including spent fuel neutrons and photons, photons from (n,g) reactions and photons from activated upper/lower hardware regions of spent fuel assemblies. This model was investigated with several variance reduction (VR) techniques and satisfactory convergence of neutron and gamma (n-g) dose rates was obtained.

This paper is organized as follows. Chapter 2 provides information about the cask geometry and source data preparation. The SCALE6.1.3/MAVRIC hybrid shielding sequence, used for cask calculations, is presented in Chapter 3. The cask shielding results are given in Chapter 4, ranging from generic to detailed source description, and from analog MC simulation to an optimized one, using FW-CADIS methodology. The accidental neutron dose rates are also quantified and compared to normal dose rates. Lastly, the conclusions are given in Chapter 5, while the list of used references is provided at the end of the paper.

II. Cask source and geometry specification

The source terms of spent fuel assemblies cover two regions: the active fuel region (neutrons and gammas) and upper/lower hardware region (gammas) simulating presence of ^{60}Co originating from impurity ^{59}Co, which can be found in steel and Inconel structural materials. The ORIGEN-ARP code of SCALE6.1.3 code [4] was used to calculate multigroup n-g sources for active fuel region. A small C-program [6] was written which reads the ORIGEN output file and generates normalized n-g spectra with the associated n-g intensities (particles/s/MTU) as a function of time. The broad-group library "v7-27n19g" was used for ORIGEN calculations, matching format of the broad shielding library used by Monaco MC module [4]. The quantities of structural material in the top, plenum and bottom hardware regions of FA are taken from reference [2] and presented in Table 1. The curies of ^{60}Co per kg of steel were 10 Ci/kg (bottom nozzle), 2.5 Ci/kg (top nozzle) and 4.6 Ci/kg (plenum), so total curie loadings were 24.1 Ci (top endfitting + plenum) and 58.9 Ci (bottom endfittings).

Mario Matijević, Matej Pekeč, Hybrid Shielding Calculations of GBC32 Cask, Journal of Energy, vol. 75 Number 1 (2026), 3–8
https://doi.org/10.37798/2026751724

Scientific paper
Manuscript received February 6, 2026; revised March 6, 2026; accepted March 13, 2026

TABLE I.
FUEL ASSEMBLY HARDWARE PARTS AND MATERIALS

FA part	Weight (kg) / FA	Zone	Material
Bottom nozzle	5.897	bottom	Stainless steel 304
Hold-down spring	0.960	top	Inconel 718
Spacer – plenum	0.885	gas plenum	Inconel 718
Top nozzle	6.890	top	Stainless steel 304
Grid sleeve	0.091	gas plenum	Stainless steel 304

The generic cask source has only one fuel zone (32 fuel elements of OFA Westinghouse 17x17 type) with an averaged values of: enrichment e=4.0%, burnup BU=45.0 GWd/MTU, cooling time=10 years, specific power=40.0 MW/MTU, and uranium weight of 0.4634 MTU per FA [5]. The pellet density was 10.357 g/cm^3 with 94.5% theoretical value, and moderator density was 0.71 g/cm^3. The ORIGEN-ARP [3] was used to make burnup-depletion calculations (12 cases in total), using three cross section libraries per irradiation cycle and one library for a decay cycle. For a generic neutron case, one fuel zone with total of 7.718e+09 n/s was defined while a generic photon case had multiple gamma sources: one fuel zone with total of 1.136e+17 phot/s and three hardware regions (bottom nozzle, upper nozzle and plenum) giving additional 3x32 or 96 distributed ^{60}Co sources.

The more realistic cask source has 32 FAs in 3 different fuel zones, with zone-wise neutron/gamma spectra and particle intensities calculated by ORIGEN-ARP module:

- Zone 1 (red): 8 FA, BU=48 GWd/MTU, e=4.5%, cooling time = 14 years
- Zone 2 (blue): 12 FA, BU=40 GWd/MTU, e=3.6%, cooling time = 12 years
- Zone 3 (white): 12FA, BU=30 GWd/MTU, e=3.0%, cooling time=30 years

The specific thermal power was assumed to be 36.0 MW/MTU. This more realistic source description introduces an extra burden on source sampling routines during Monaco MC simula-tions, taking more CPU time. The comparison of a generic and realistic cask source is shown in Figure 1.

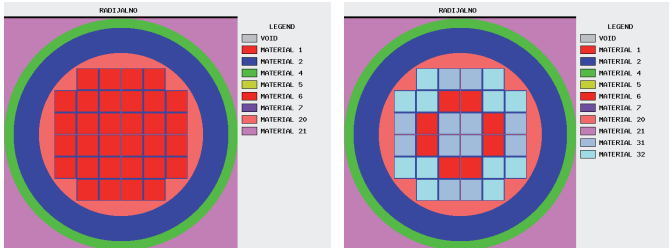

Fig. 1. Generic (left) and more realistic (right) cask source description

An important factor for radiation shielding characterization of the cask was inclusion of an axial normalized burnup profile, producing a biased sampling of source neutrons and photons along the active fuel length (Figure 2). This ultimately leads to a more realistic, asymmetrical dose distributions. This function in form of binned histogram was imported from the reference [1] and total of 18 fuel axial segments with corresponding probabilities were included in the MAVRIC cask model. The same burnup profile was used for sampling neutrons and photons, which is a reasonable approach.

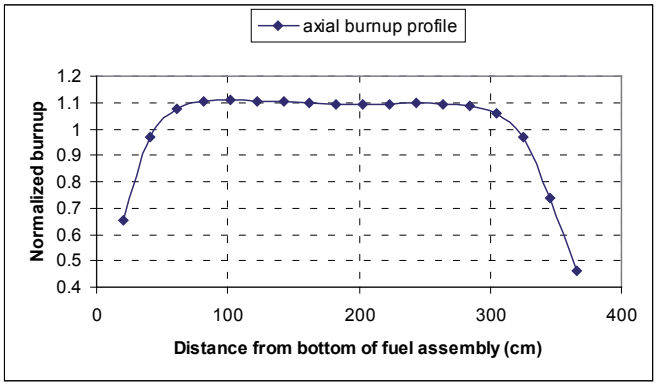

Fig. 2. Axial burnup profile of the spent fuel

The sources of fuel assemblies are thus spatially distributed, forming sources from the active fuel region and from the upper/lower hardware regions. These sources can be further broken into neutron and gamma-ray components, with separate intensities and spectrum. The active fuel region is a neutron-gamma emitter while the hardware region contains only gamma sources from activated ^{60}Co (steel impurity). The neutron-gamma sources in active FA region were calculated using ORIGEN-ARP code, using previously generated cross section libraries for OFA fuel [5]. Gamma sources for fuel assembly hardware parts were calculated using industry values i.e. the curies of cobalt per kg of specific steel part. Figure 3 shows MAVRIC model of the GBC-32 cask for a normal transport condition, while accidental case assumes removal of the resin (green layer) from the model. The truncated model on the right has a helium gas removed around FA cells for clarity. Also, this model corresponds to a realistic cask source with three FA zones. The FAs were homogenized by isotopic mass preservation and modelled as stacked axial layers. To be more precise, the fuel, cladding and hardware volume fractions were smeared over the FA basket. The cask body dimensions are taken from reference [2] and given in Table 2.

TABLE II.
CASK GLOBAL DIMENSIONS

Model section	Radius (cm)	Total height (cm)
Cavity (He gas)	87.5	425.76
Steel shell	114.5	495.76
Resin shell	124.5	376.00

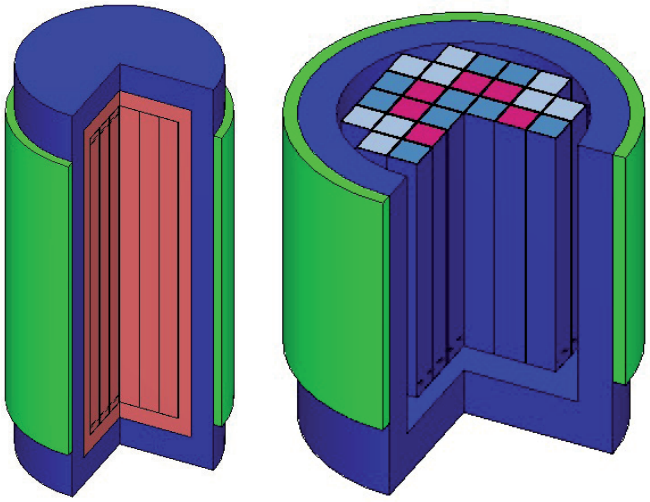

Fig. 3. MAVRIC model of the GBC-32 cask with a three FA zones

Mario Matijević, Matej Pekeč, Hybrid Shielding Calculations of GBC32 Cask, Journal of Energy, vol. 75 Number 1 (2026), 3–8
https://doi.org/10.37798/2026751724

Scientific paper
Manuscript received February 6, 2026; revised March 6, 2026; accepted March 13, 2026

III. SCALE6.1.3 SHIELDING COMPUTATIONAL TOOLS

The SCALE6.1.3 code's main shielding sequence is MAVRIC, based on the CADIS [7] and FW-CADIS [8] methods utilizing SN solver Denovo [9] for deterministic VR calculation and subsequent accelerated MC Monaco particle transport [4]. For both CADIS and FW-CADIS, the particle average weight is inversely related to an adjoint flux [10] value throughout phase-space, so locations of high importance (i.e. high adjoint flux) will have low-weighted particles and vice versa. This implies that adjoint source location for optimized MC results will represent spatial attractor for the source particles, giving »reasonable« MC results in-between regions. Depending on the volumetric size and placement of the adjoint source, it is possible to produce MC results with reasonable statistics even between the forward source and the adjoint source, but it is highly case-specific.

The detector response is found by integrating the product of the detector cross-section $\sigma_d(\vec{r},E)$ and flux over detector volume V_D:

$$R=\int_{V_D}\int_E \sigma_d(\vec{r},E)\phi(\vec{r},E)dVdE \tag{1}$$

Alternatively, if we approximate the adjoint scalar flux with a quick SN solution, where the adjoint source is set as $q^\dagger(\vec{r},E)=\sigma_d(\vec{r},E)$, then the detector response is found by integrating the product of the forward source $q(\vec{r},E)$ and the adjoint flux $\phi^\dagger(\vec{r},E)$ over the source volume V_S:

$$R=\int_{V_S}\int_E q(\vec{r},E)\phi^\dagger(\vec{r},E)dVdE\,. \tag{2}$$

The biased source distribution $\hat{q}(\vec{r},E)$ is thus based on an estimate of the adjoint scalar flux, from which the response R can be made using Eq. (2):

$$\hat{q}(\vec{r},E)=\frac{\phi^\dagger(\vec{r},E)q(\vec{r},E)}{R}=\frac{\phi^\dagger(\vec{r},E)q(\vec{r},E)}{\int_{V_S}\int_E q(\vec{r},E)\phi^\dagger(\vec{r},E)dVdE}, \tag{4}$$

where $\phi^\dagger(\vec{r},E)$, $q(\vec{r},E)$ and R are the scalar adjoint function, the source emission probability (forward source), and the total detector response, respectively [4]. For transport biasing the weight window technique is employed, that is, space-energy dependent geometric splitting/roulette. Biased source and weight-window lower bounds are consistent, so the source particles are created with statistical weights within weight windows:

$$\overline{w}(\vec{r},E)=\frac{q(\vec{r},E)}{\hat{q}(\vec{r},E)}=\frac{R}{\phi^\dagger(\vec{r},E)}=\frac{\int_{V_S}\int_E q(\vec{r},E)\phi^\dagger(\vec{r},E)dVdE}{\phi^\dagger(\vec{r},E)}. \tag{5}$$

The inverse relationship between particle statistical weight and adjoint function is crucial, implying more splitting of low-weighted particles in important regions of the MC model. The dose mapping of the cask involves calculation of near and far detector dose rates, so FW-CADIS methodology was selected for this problem. To expedite many simulation cases, Denovo SN solver [11] was used with "basic" FW-CADIS parameters: S4 quadrature set, P1 scattering cross section expansion (Legendre order), step characteristic (SC) spatial differencing, and diagonal transport correction. The macromaterial option mixed cca 10 pure materials into 3-4 times more pseudomaterials (case dependent) on uniform SN mesh with 768e3 cells covering global unit. Even a low-quality deterministic solution will be a good enough approximation for biasing the final MC simulation. The adjoint source was always defined as dry air external to the cask with spectrum corresponding to dose rate function (9029-neutrons or 9504-photons). Monaco MC was used with 5e6 histories and shielding library was "v7-27n19g" for both SN and MC portions of calculations [12]. The cylindrical mesh tally with 150e6 cells was used for capturing global n-g dose rates.

IV. GBC-32 CASK SHIELDING RESULTS

The shielding evaluation of the GBC-32 cask is done by calculating n-g dose rates in axial and radial direction of the cask, to demonstrate compliance with 10CFR71 regulatory limits on dose rates during normal and accidental cask transport. These limits are 2 mSv/h (200 mrem/h) at the cask surface and 0.1 mSv/h (10 mrem/h) at 2 m from the cask. The same dose rates under hypothetical accidental scenario have higher dose limits of 10 mSv/h (1000 mrem/h) at 1 m from the cask surface. The accidental cask model has impact limiters and neutron resin shield removed.

The shielding analysis was performed by using SCALE6.1.3/MAVRIC sequence for optimized 3D MC calculations of cask's radiation field. The obtained results show compliance with 10CFR71 regulatory limits in all cases. The cylindrical mesh tally was used to capture n-g global flux convergence and derived n-g dose rates (in rem/h) around the cask exterior. Additionally, point detectors were placed in cask midplane, extending radially from cask's surface to 2 m distance using steps of 50 cm.

A. MAVRIC RESULTS FOR ANALOG MC AND GENERIC CASK SOURCE

Figures 4 to 6 show analog MC results of neutron dose rates - neutrons penetrate more easily through 35 cm thick SS304 shield compared to gamma-rays, but statistical noise is still unacceptably high in obtained dose axial profiles (Figure 5). The neutron dose maximum is in upper and lower cask region, reaching values above the 0.1 rem/h. The Monaco MC module was used with 500 batches and 2000 neutrons per batch using broad shielding library "v7-27n19g". For photon case, with noticeable slow MC convergence, these values were higher, i.e. 5000 batches and 10000 per batch. The total CPU time was 650 min for neutrons and 716 min for photons. Compared to neutrons, photons are unable to penetrate outer steel body of the cask, leaving the exterior without the results (Figure 6).

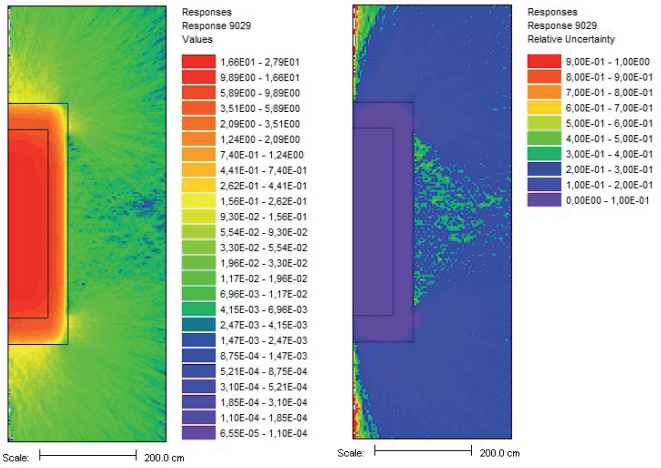

Fig. 4. Neutron dose rates (rem/hr) with errors (analog MC)

Mario Matijević, Matej Pekeč, Hybrid Shielding Calculations of GBC32 Cask, Journal of Energy, vol. 75 Number 1 (2026), 3–8
https://doi.org/10.37798/2026751724

Scientific paper
Manuscript received February 6, 2026; revised March 6, 2026; accepted March 13, 2026

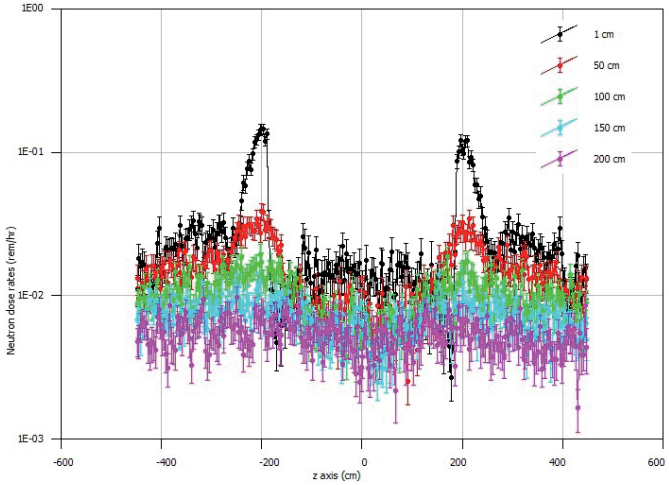

Fig. 5. Neutron dose (rem/h) axial profiles (analog MC)

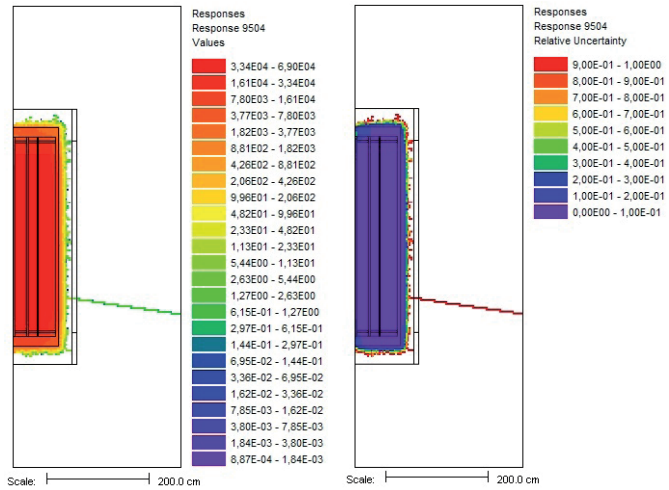

Fig. 6. Photon dose rates (rem/hr) with errors (analog MC)

B. MAVRIC Results for FW-CADIS and Generic Cask Source

The same n-g shielding calculations were repeated by using FW-CADIS methodology of MAVRIC shielding sequence. Total CPU time was 404 min for neutron case and 921 min for photon case. The number of particles simulated was the same as in analog cases. The FW-CADIS variance reduction technique was used to improve the overall transport of neutrons and photons. Figures 7 and 8 show significant improvement in MC statistics and neutron dose distribution, which can also be seen in axial and radial curve profiles for different distances from the cask. As expected, the neutron streaming is pronounced near upper and lower cask region, reaching maximum about 0.01 rem/h at the cask surface, well below regulatory limit of 0.2 rem/h. For a 2 m dose limit (0.01 rem/h), Figure 7 also depicts dose rates above that limit, indicating compliance with regulations.

Figures 9 and 10 show optimized distribution of gamma doses for FW-CADIS and generic source, with an axial and radial dose profiles; the dose difference between upper and lower cask plates are due to axial burnup profile function which was used for source particle biasing. The dose limits by 10CFRPart71 are again met, even though photon simulation exhibits a slow MC convergence.

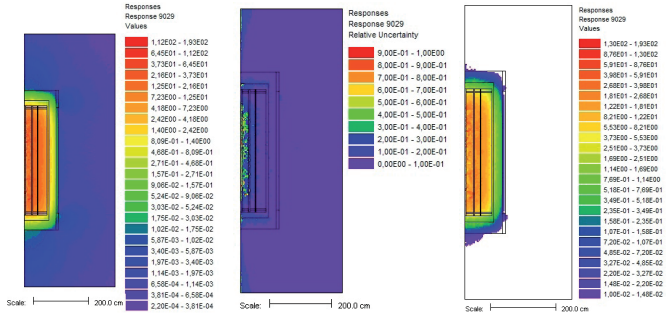

Fig. 7. Neutron dose rates (rem/h) with errors and values above the 2 m regulatory limit

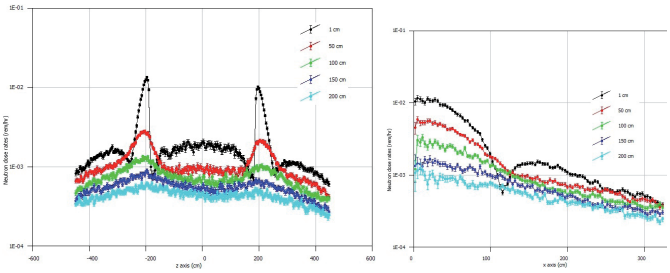

Fig. 8. Neutron dose rates (rem/h) axial and radial profiles (generic source)

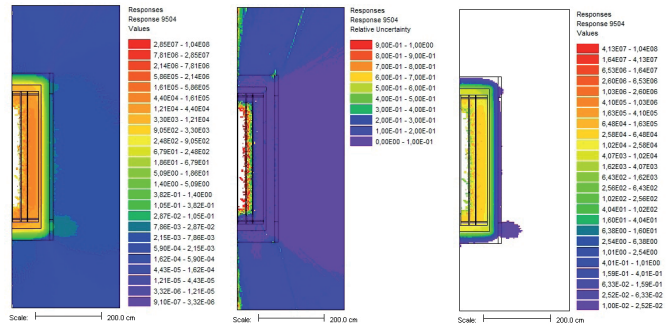

Fig.9. Gamma dose rates (rem/hr) with errors and values above the 2 m regulatory limit

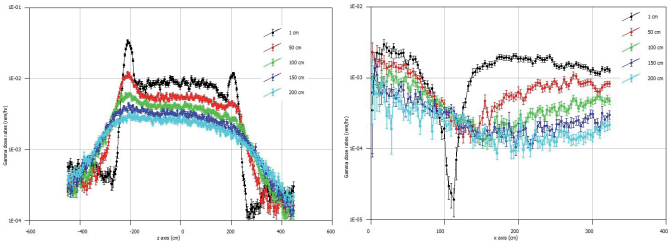

Fig. 10. Gamma dose rates (rem/h) axial and radial profiles (generic source)

C. MAVRIC Results for FW-CADIS and Realistic Cask Source

This set of n-g calculations is addressing a more realistic cask source with a three fuel regions or zones, where each zone is described with specific (averaged) values of fuel enrichment, burnup and cooling time. The zonal values were taken as representative, real-life cases. These MC calculations are more complex, since biased source sampling is performed using 3-zonal particle spectra for active fuel, hardware activation spectrum for 3 axial regions per FA and axial burnup profile for spatial biasing, making distinction between neutrons and gammas. The MC and SN parameters remain in the same as in previous calculations.

Mario Matijević, Matej Pekeč, Hybrid Shielding Calculations of GBC32 Cask, Journal of Energy, vol. 75 Number 1 (2026), 3–8
https://doi.org/10.37798/2026751724

Figure 11 shows results of neutron dose rates (rem/h) calculated by FW-CADIS for three-zone fuel pattern, clearly influencing dose profiles in axial direction of the cask, shown in Figure 12. Additionally, the values above the dose regulatory limit for 2 m distance (0.01 rem/h) from the cask are also shown in Figure 11, clearly indicating compliance with the limit. As expected, the dose maximum corresponds to a region with a least attenuating material, which are typically ventilation openings. The difference in upper and lower dose maximum are due to inclusion of axial burnup profile used as a spatial sampling function.

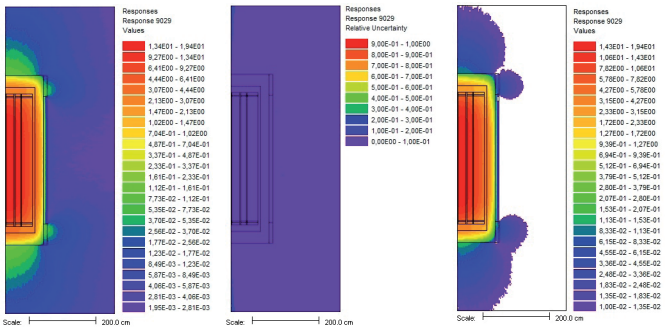

Fig. 11. Neutron dose rates (rem/hr) with errors and values above the 2 m regulatory limit

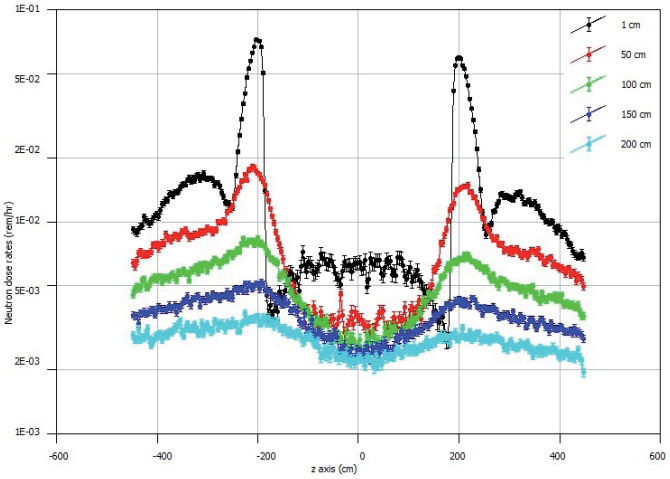

Fig. 12. Neutron dose rates (rem/h) axial profiles (realistic source)

Figure 13 shows results of gamma dose rates (rem/h) calculated by FW-CADIS for three-zone fuel pattern, again influencing dose profiles in axial direction of the cask, shown in Figure 14. The values above the dose regulatory limit for 2 m distance (0.01 rem/h) from the cask are again shown in Figure 13, clearly indicating compliance with the regulatory limit. The dose rates maximum again corresponds to upper and lower cask regions, while the difference in upper and lower dose maxima are due to inclusion of axial burnup profile.

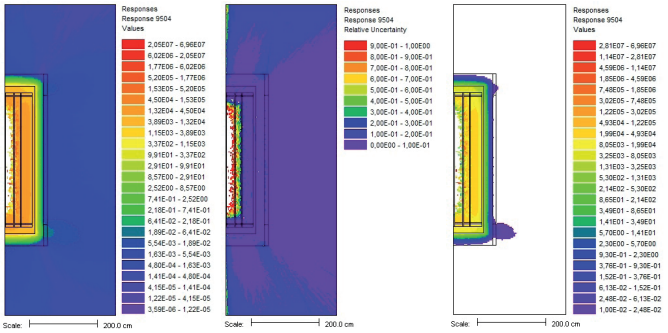

Fig. 13. Gamma dose rates (rem/hr) with errors and values above the 2 m regulatory limit

One should also notice an excellent MC dose rate convergence by FW-CADIS method, in both neutron and gamma case, covering almost uniformly the simulation model with particles. The global unit has dimensions of 6.5x6.5x9 m, where cask dimensions are cca 5 m in height and 2.5 m in diameter. The CPU time for neutron dose case was 3.6 hr (SN) and 30 hr (MC), and for gamma dose case was 1.0 hr (SN) and 29 hr (MC).

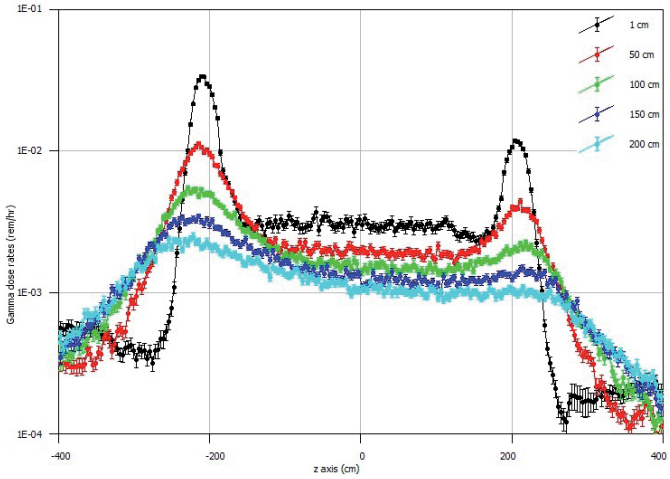

Fig. 14. Gamma dose rates (rem/h) axial profiles (realistic source)

Summary of neutron and gamma dose rates on point detectors (PDs) with variable radial distance in the cask midplane are presented in Table 3 for all simulated n-g cases. The abbreviated names for cases are the following: "generic" is for a uniform (one fuel zone) source, "realistic" is for a nonuniform (three fuel zones) source, "analog" is for MC without VR parameters, and "FW-CADIS" is for deterministically obtained VR parameters. The FAs in outer region (or zone) of the cask basket are basically driving the received dose rates since interior sources are being self-shielded.

TABLE III.
SUMMARY OF DOSE RATES (REM/HR) IN CASK MIDPLANE

PD	Neutrons (generic, analog)	Neutrons (generic, FW-CADIS)	Neutrons (realistic, FW-CADIS)	Photons (generic, analog)	Photons (generic, FW-CADIS)	Photons (realistic, FW-CADIS)
1.	1.2e-2±35%	1.0e-3±25%	8.0e-3±20%	9.6e-3±91%	9.5e-3±8.5%	6.4e-3±6.9%
2.	8.4e-3±3.8%	6.6e-4±2.8%	3.9e-3±1.8%	1.9e-3±49%	6.5e-3±1.8%	3.4e-3±1.7%
3.	6.4e-3±2.3%	5.3e-4±1.7%	3.0e-3±0.7%	6.5e-3±84%	4.6e-3±1.3%	2.3e-3±1.1%
4.	5.6e-3±1.9%	4.6e-4±1.9%	2.6e-3±0.5%	8.2e-3±91%	3.5e-3±1.0%	1.8e-3±1.0%
5.	4.8e-3±1.4%	3.8e-3±1.1%	2.3e-3±0.5%	8.5e-3±93%	2.8e-3±0.9%	1.4e-3±0.8%

D. MAVRIC Results for Accidental Case

This last set of calculations presents shielding evaluation of the accidental cask condition, where neutron dose rates clearly meet the regulatory limit of 10 mSv (1 rem/h) at 1 m from the cask surface. The MC simulation model is the same as in the previous section (realistic source using FW-CADIS), but with the impact limiter (wood) and neutron shield (resin) removed from the cask body exterior. It is assumed how this modification will make a marginal effect on photon transport, so only a neutron simulation was performed.

The effect of wood and resin removal is clearly seen in Figure 15, with augmented dose rates around the cask body by streaming neutrons. One can notice maximum of dose rates shifting from vent openings to the cask midplane in Figure 16. However, this is still below the regulatory limit, which can be seen in Figure 15 using the threshold operator, setting the minimum dose values to 1 rem/h.

Mario Matijević, Matej Pekeč, Hybrid Shielding Calculations of GBC32 Cask, Journal of Energy, vol. 75 Number 1 (2026), 3–8
https://doi.org/10.37798/2026751724

The dose rates profiles along the cask axial dimension, for different distances from the cask surface, are shown in Figure 16. The neutron dose rates peak at the cask midplane with surface, 1m and 2 m neutron dose values corresponding to 0.2 rem/h, 0.09 rem/h and 0.04 rem/h.

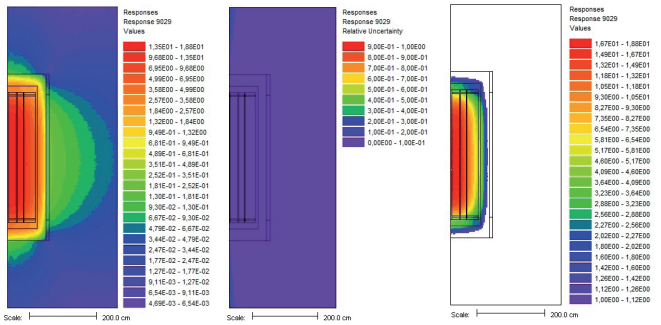

Fig. 15. Neutron dose rates (rem/hr) with errors and values above the 1 m regulatory limit

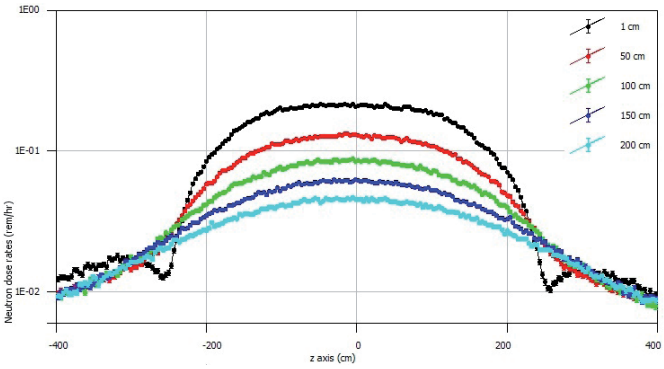

Fig. 16. Neutron dose rates (rem/h) axial profiles (accidental case)

Additional effort was put in visualisation of ratio accidental-to-normal neutron dose rates, by using MAVRIC auxiliary programs for mesh tally object formatting. The user has an option to split mesh tally object into independent families and to divide their values. Such relative ratio of neutron dose rates is shown in Figure 17 with an extra 3D plot using VisIt code [13], showing maximum jump of cca 50 in relative dose ratio at the cask surface in axial direction.

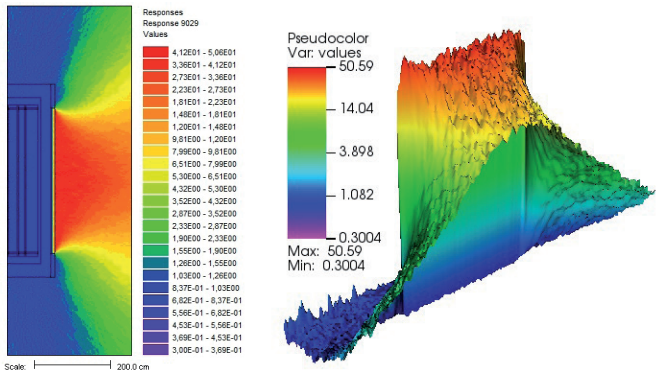

Fig. 17. Neutron dose rates relative ratio (accidental-to-normal)

Conclusion

The shielding performance of GBC-32 cask was quantified to demonstrate compliance with the dose rate limits of 10CFRPart71 for normal and accidental conditions. For that purpose, two different levels of detail were used for the source specification: a generic source (1 fuel zone) and more realistic source (3 fuel zones), using averaged values for enrichment, burnup and cooling time. An analog MC simulation was first performed, giving low quality MC results with a high statistical noise, especially for photon case. To remedy this situation, the FW-CADIS method was used to optimise neutron-gamma radiation field and dose rates around the cask, taking previously prepared source terms with ORIGEN-ARP module. The multisource problem included spent fuel neutrons and photons, photons from (n,g) reactions and photons from activated upper/lower hardware regions of spent fuel assemblies. The presented MC dosimetry results correspond to normal cask conditions, but an accidental scenario was also investigated, for which the resin neutron shield was removed from the shielding configuration. The obtained dose rate values proved to be well below regulatory limits, indicating compliance of the cask shielding design under normal and accidental conditions.

Acknowledgement

The work was carried out as part of the project HRZZ-IP-2024-05-4011 of the Croatian Science Foundation.

References

[1] "Computational Benchmark for Estimation of Reactivity Margin from Fission Products and Minor Actinides in PWR Burnup Credit", Prepared by J. C. Wagner, NUREG/CR-6747, ORNL/TM-2000/306.

[2] "Recommendations for Shielding Evaluations for Transport and Storage Packages", NUREG/CR-6802, ORNL/TM-2002/31, Prepared by B. L. Broadhead.

[3] "OrigenArp Primer: How to Perform Isotopic Depletion and Decay Calculations with SCALE/ORIGEN", prepared by S. M. Bowman, I. C. Gauld, ORNL/TM-2010/43.

[4] "SCALE: A comprehensive Modeling and Simulation Suite for Nuclear Safety and Design", ORNL/TM-2005/39, Version 6.1, June 2011. Available from Radiation Safety Information Computational Center at Oak Ridge National Laboratory as CCC-785.

[5] M. Matijević, M. Pekeč, "Characterization of the GBC-32 Fuel Assembly Source Terms", Vol. 71, No. 4 (2022), Journal of Eenergy - ENERGIJA (04/2022), https://doi.org/10.37798/2022714467

[6] B.W. Kernighan, D.M. Ritchie, The C Programming Language, 2nd Edition, Prentice Hall, 1988.

[7] J. C.Wagner and A. Haghighat, "Automated variance reduction of Monte Carlo shielding calculations using the discrete ordinates adjoint function," Nuclear Science and Engineering, Vol. 128, no. 2, pp. 186–208, 1998.

[8] J. C. Wagner, E. D. Blakeman, and D. E. Peplow, "Forward weighted CADIS method for global variance reduction," Transactions of the American Nuclear Society, vol. 97, pp. 630–633, 2007.

[9] T. M. Evans, A.S. Stafford, R.N. Slaybaugh, K.T. Clarno, "Denovo: A New Three-Dimensional Parallel Discrete Ordinates Code in SCALE," Nuclear Technology, 171:2, 171-200, DOI: 10.13182/NT171-171, 2010.

[10] G. I. Bell and S. Glasstone, "Nuclear Reactor Theory," Van Nostrand Reinhold Company, Litton Educational Publishing, 1970.

[11] E. E. Lewis, W. F. Jr. Miller, "Computational Methods of Neutron Transport", American Nuclear Society, Illinois, 1993.

[12] M. B. Chadwick, P. Obložinsky, M. Herman et al., "ENDF/B-VII.0: next generation evaluated nuclear data library for nuclear science and technology," Nuclear Data Sheets, Vol. 107, no. 12, pp. 2931–3060, 2006.

[13] VisIt: An End-User Tool for Visualizing and Analyzing Very Large Data, VisIt User's Manual, Version 1.5, UCRL-SM-220449, Lawrence Livermore National Laboratory, Weapons and Complex Integration, 2005.

Mario Matijević, Matej Pekeč, Hybrid Shielding Calculations of GBC32 Cask, Journal of Energy, vol. 75 Number 1 (2026), 3–8
https://doi.org/10.37798/2026751724

Scientific paper
Manuscript received November 26, 2025; revised December 4, 2025; accepted January 14, 2026

Journal of Energy

VOLUME 75 Number 1 | 2026

journal homepage: http://journalofenergy.com/

Natural Heat Transfer Performance of Helium Filled Spent Fuel Multi Purpose Container Calculated for Different Initial Pressures

Davor Grgić, Nikola Novosel, Paulina Družijanić, Petra Strmečki

***Summary* — The simple model of helium filled Holtec's Multi Purpose Container (MPC) for 37 spent fuel assemblies was developed and the calculation was performed using the Ansys Fluent code in steady state. The flow and temperature distribution within the MPC was calculated for different initial helium pressures, and for limiting cask heat loading found in the NPP Krsko SFDS (Spent Fuel Dry Storage) campaign number 1. The determined relationship between helium top to bottom temperature increase and helium pressure decrease can be used as a measure of cask leakage. In addition, lateral temperature distribution in the top MPC plenum, influenced partially by different spent fuel assembly loading, should be checked as a cause for temperature variation at the MPC external top surface, where RTD (Resistance Temperature Detector) detectors are installed.**

***Keywords* — Spent fuel dry storage, MPC internal natural circulation, helium pressure, Fluent**

I. Introduction

Nuclear Power Plant Krško decided to store its spent fuel in the Spent Fuel Dry Storage (SFDS). The SFDS consists of a Dry storage building (DSB) which may house up to 70 HI-STORM storage casks and HI-TRAC transfer cask is used for transferring the spent fuel from the spent fuel pool to the DSB. The fuel is placed in an interchangeable Multi-Purpose Container (MPC) which can fit both HI-STORM and HI-TRAC. The spent fuel transfer to the DSB is divided into four loading campaigns. In the first loading campaign, which was in 2023, 592 spent fuel assemblies were transferred. The second loading campaign is expected to start in 2028 during which another 592 spent fuel assemblies will be transferred [1].

MPC is a stainless-steel structure which can house up to 37 spent fuel assemblies. The fuel is inserted into a METAMIC-HT basket supported by aluminium shims. After being filled with spent fuel and dried out, the MPC is sealed with a welded lid to form a confinement boundary and backfilled with helium to the design-basis pressures. The MPC basket has flow holes at the bottom to ensure helium circulation. Helium is an inert gas, so it provides stable environment for long-term storage of the spent fuel and it ensures passive heat transfer from the spent fuel to the MPC. The heat transfer within MPC and when canister is inserted in HI-STORM cask is shown in Figure 1. Heat generated within the spent fuel rods is transferred by conduction from the inner wall to the outer wall of the cladding. The outer wall of the cladding is in contact with helium, therefore natural convection occurs as helium heats up. The heated helium rises within square storage cells towards the top of the MPC, transfers part of the heat to the top of the MPC (top lid) and descends towards the bottom of the MPC through a downcomer formed by a basket outer surface and an MPC wall inner surface. The heat that reaches the inner side of the MPC wall is transferred by conduction to the outer surface of the MPC. The air removes heat from the MPC outer side by natural convection. Except for natural convection and conduction, radiation heat transfer also occurs, but to a lesser extent, therefore it is often neglected in normal operating conditions [2].

Since helium plays a vital role in the thermal performance of the MPC, it should be retained within the MPC and not diluted by the air ingress (air has lower thermal conductivity and it is not inert gas). Therefore, it is important to have a means to detect the situation caused by possible helium leakage [3].

In this paper, the simple model of helium filled Holtec's MPC for 37 spent fuel assemblies was developed and the calculation was performed using the Ansys Fluent code in steady state. The flow and temperature distribution within the MPC was calculated for different initial helium pressures, and for limiting cask heat loading found in the NPP Krsko SFDS campaign number 1. The obtained relationship between helium top to bottom temperature increase and helium pressure decrease could be used as a measure of cask leakage. In addition, lateral temperature distribution in the top MPC plenum, influenced partially by different spent fuel assembly (FA) heat loading, should be checked as a cause for temperature variation at the MPC external top lid surface, where upper RTD (Resistance Temperature Detector) detectors are installed.

(Corresponding author: Davor Grgić)

Davor Grgić, Nikola Novosel, Paulina Družijanić and Petra Strmečki are with the University of Zagreb Faculty of Electrical Engineering and Computing, Zagreb, Croatia (email: davor.grgic@fer.unizg.hr, nikola.novosel@fer.unizg.hr, paulina.druzijanic@fer.unizg.hr, petra.strmecki@fer.unizg.hr).

Davor Grgić, Nikola Novosel, Paulina Družijanić, Petra Strmečki, Natural Heat Transfer Performance of Helium Filled Spent Fuel Multi Purpose Container Calculated for Different Initial Pressures, Journal of Energy, vol. 75 Number 1 (2026), 9–17
https://doi.org/10.37798/2026751726

Fig. 1. Passive cooling of MPC and HI-STORM storage cask

II. Methodology Description

A. Ansys Fluent

Ansys Fluent is a general-purpose computational fluid dynamics (CFD) software used to model fluid flow, heat and mass transfer, chemical reactions, and similar processes. We used release 2020R2 of the code [4]. Fluent is known for its advanced physics modelling capabilities, which include turbulence modelling, single and multiphase flows, combustion, battery modelling, fluid-structure interaction, and much more. Also known for its efficient HPC (High Performance Computing) scaling, large models can easily be solved in Fluent on multiple processors on either CPU (Central Processing Unit) or GPU (Graphical Processing Unit). Multiple solver options are available, including pressure-based and density-based solvers to cover low-speed to hypersonic flows.

Ansys Fluent uses finite volume method (FVM) to solve complex engineering problems. The modeling method includes three phases

1. **Pre-process:** Define the physics and real-world conditions to be used in the model.
2. **Mesh and Solve:** Divide the object into finite volumes via meshing and apply the relevant physics representations and/or equations to each element. Then assemble the equations and solve them.
3. **Post-process:** Compute results to analyze and interpret implications for the whole domain.

B. MPC Modelling in Ansys Fluent

The model developed for the evaluation of the thermal performance of the MPC consists of the MPC body, basket, shims and spent fuel assemblies as shown in Figure 2. MPC is an empty cylinder with top and bottom lid. The outer diameter of the MPC is about 1.9 m and shell thickness is about 1.3 cm. Bottom and top lid thicknesses are about 7.6 cm and 22.9 cm, respectively. The basket is placed at the bottom of the MPC. It has 37 positions (square cells) for the spent fuel assemblies. Each location has flow holes at the bottom of the basket to ensure natural circulation of helium. The basket is supported at the periphery by aluminium shims, of the different shape, which increase the lateral thermal conduction transfer toward the MPC wall and ensure stability of the basket.

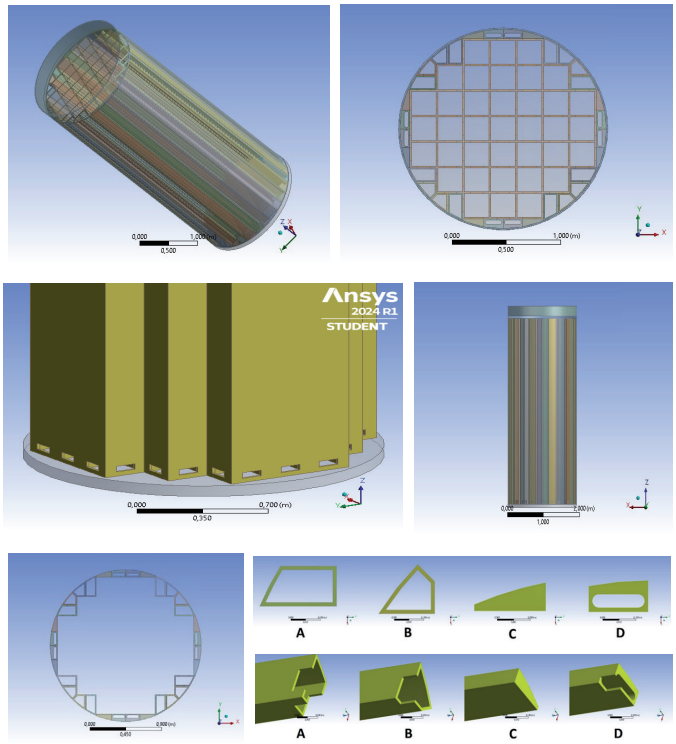

Fig. 2. MPC model in Ansys

C. Assumptions and Settings

Spent fuel assemblies that are placed in the MPC are the NPP Krško 16x16 fuel assemblies with 235 fuel rods, 20 guide tubes for control rods, and 1 instrumentation guide tube [5]. Two modelling approaches were used in this research study. The first one is an explicit model which is based on a model of each fuel rod in a fuel assembly (Figure 3). The rod diameter is 9.5 mm, height 3.66 m, and the distance between the fuel rod centres is 1.2 cm. In this model, guide tubes, distance lattice and upper and lower nozzle were neglected. This model is more complex, and calculations are computationally demanding. The other spent fuel assembly model is based on the thermal equivalent cylinder (Figure 4). This mo-del is simplified in a way that instead of 235 fuel rods, one rod is modelled representing all 235 fuel rods (r_1), with the equivalent ra-dius (r_{eq}) of 7.3 cm calculated using the Equation 1. That way flow

Davor Grgić, Nikola Novosel, Paulina Družijanić, Petra Strmečki, Natural Heat Transfer Performance of Helium Filled Spent Fuel Multi Purpose Container Calculated for Different Initial Pressures, Journal of Energy, vol. 75 Number 1 (2026), 9–17
https://doi.org/10.37798/2026751726

cross section of the channel is preserved, but heat transfer surface area is underestimated (affects both pressure drop and temperature of the cylinder).

$$r_{eq} = \sqrt{r_1^2 \cdot n} \quad (1)$$

The following assumptions were made regarding material assignment. MPC bottom and top lid, and body were modelled as stainless steel, while basket, inserts and fuel rods were assumed to be made of aluminium. Although fuel rods are made of uranium and cladding is made of Zircaloy, the assumed aluminium, having good thermal conductivity, is used to compensate for the reduced heat transfer surface area in the equivalent model. The rest of the free space within the MPC is filled with helium. The material properties are standard material properties widely used in technical literature, provided in Table 1.

Fig. 3. NPP Krško fuel assembly explicit model in Ansys

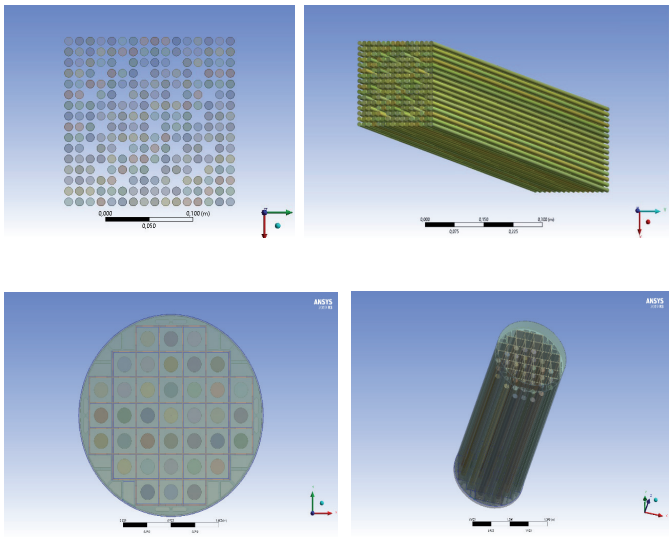

Fig. 4. MPC geometry with fuel assembly equivalent model in Ansys

TABLE I.
MATERIAL PROPERTIES

Material	Density	Thermal conductivity
Helium	Ideal gas	0.152 W/(m•K)
Aluminium	2719 kg/m³	202.4 W/(m•K)
Stainless steel	8030 kg/m³	16.27 W/(m•K)

The following settings were used for the heat transfer simulation [6]:

- Steady state (pseudo transient) solver
- Gravity is taken into account
- Turbulent fluid flow (k-epsilon SST model)
- The initial temperature of helium is 293 K, and the initial pressure of helium is 4 bar, the properties are temperature dependent (full density model)
- Volumetric heat generated within fuel element is set to 11.287 kW/m³ (one fuel element produces 687 W, for 37 fuel elements that is 25.4 kW)
- Fixed temperature of 293 K at the bottom of the MPC bottom lid
- Ambient temperature is 293 K
- Assumed convective heat transfer coefficient on the outer surface of the top lid 5 W/(m²K) and on the outer surface of the MPC body 10 W/(m²K).

III. RESULTS

A. EXPLICIT AND EQUIVALENT MODEL

As already mentioned, Ansys Fluent is a FVM based code, therefore the selection of the mesh size is an important part of the calculation. The larger mesh size means more accurate results, but at the expense of longer CPU time and more computational resources. The surface and volume mesh for the lower part of the MPC with the explicit and with the equivalent fuel assembly model are shown in Figure 5. Comparing the sizes of the two models, for only one spent fuel assembly at the central position, about 3 times larger number of mesh elements was needed for the explicit model. The number of cells, faces and nodes for MPC with single equivalent fuel assembly are: 9816064, 63423309 and 51485378, respectively. The convergence of the calculation is shown in Figure 6 for the explicit and equivalent model. The number of iterations performed was 3500 for the explicit model and 1000 for the equivalent model. Due to the less complicated geometry, the solution of the equivalent model converges faster. Figure 7 shows axial temperature distribution for the explicit and equivalent model for the central vertical plane. The maximum temperature in the explicit model is 334 K, and in the equivalent model 329 K, for the same heat load. The smaller heat transfer area in the equivalent model is more than compensated by high thermal conductivity of the aluminium. That is the reason for higher gas temperatures in internal subchannels of the explicit model. The temperature distribution of the fuel assembly in the explicit case is closer to the real case. Local temperature distribution at the MPC top lid surface is shown in Figure 8. The maximum temperature is 302 K and the temperature distribution is almost equal in both cases. Therefore, the equivalent model is good enough for the calculation of temperatures on the outer surfaces of the MPC. Flow velocity distribution is shown in Figure 9. In the explicit model the highest velocities are in the guide tubes and in the equivalent model the highest velocities are around the fuel assembly simulator surface. Due to slightly lower pressure drop in case of the equivalent model, the maximum velo-cities are higher than in the explicit model.

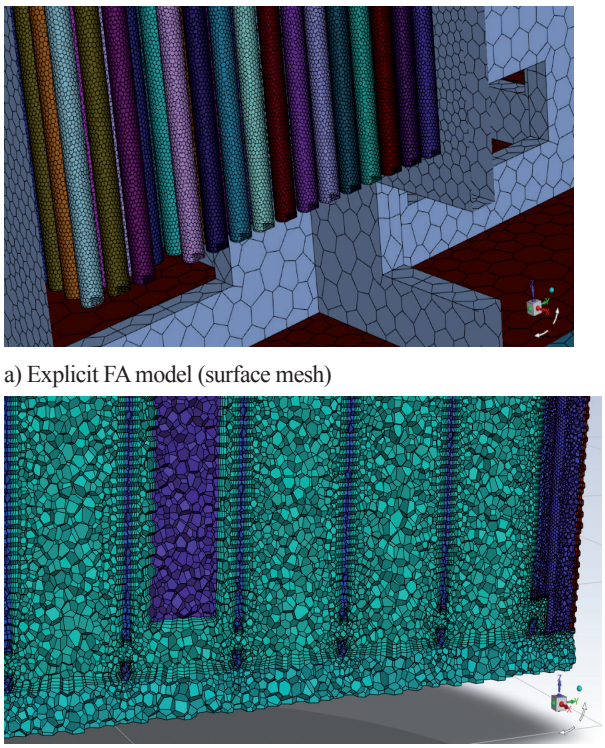

a) Explicit FA model (surface mesh)

b) Equivalent FA model (volume mesh)

Fig. 5.Surface and volume meshes of the MPC bottom

Davor Grgić, Nikola Novosel, Paulina Družijanić, Petra Strmečki, Natural Heat Transfer Performance of Helium Filled Spent Fuel Multi Purpose Container Calculated for Different Initial Pressures, Journal of Energy, vol. 75 Number 1 (2026), 9–17
https://doi.org/10.37798/2026751726

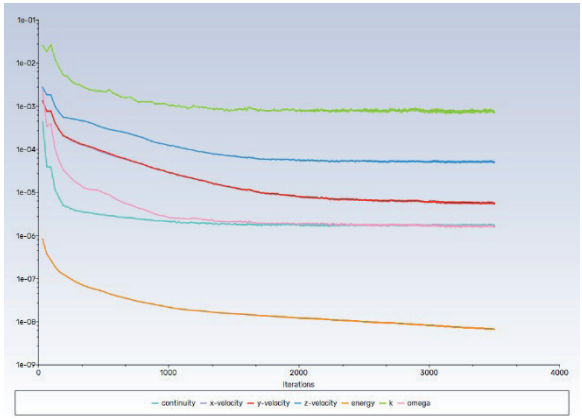

a) Explicit FA model

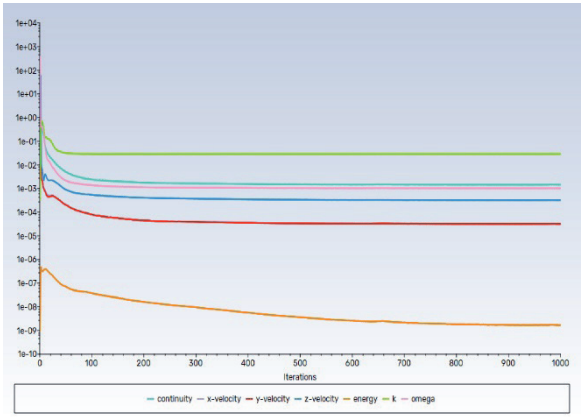

b) Equivalent FA model

Fig. 6. Convergence of the calculation

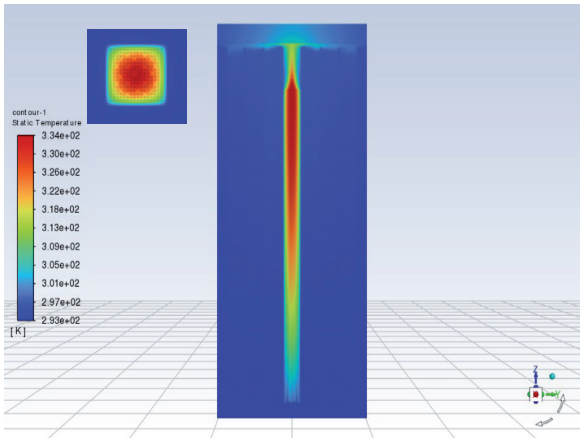

a) Explicit model

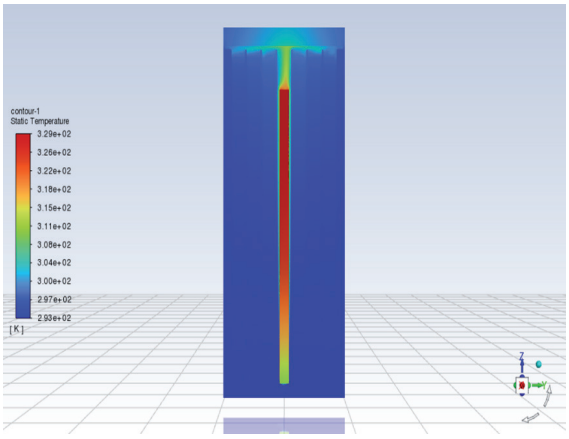

b) Equivalent model

Fig. 7. Temperature distribution for a) explicit model, and b) equivalent model

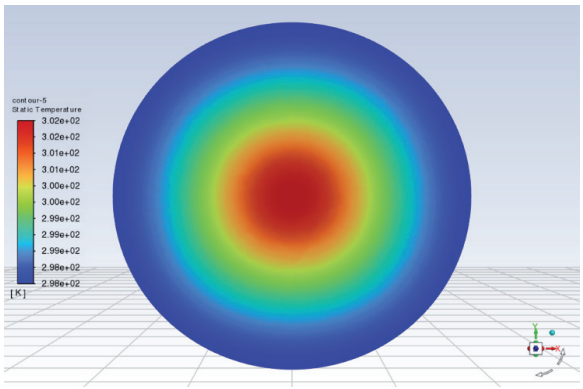

a) Explicit model

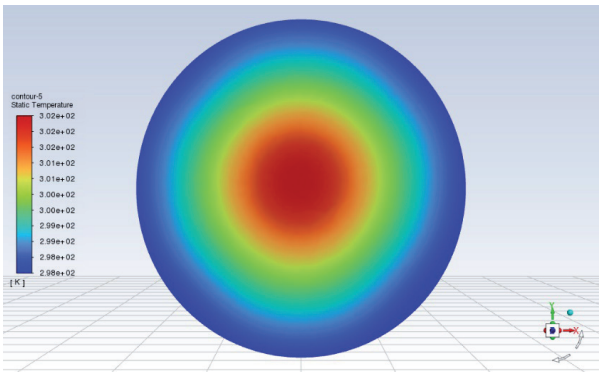

b) Equivalent model

Fig. 8. Local temperature distribution at the MPC top lid surface a) explicit model, and b) equivalent model

Davor Grgić, Nikola Novosel, Paulina Družijanić, Petra Strmečki, Natural Heat Transfer Performance of Helium Filled Spent Fuel Multi Purpose Container Calculated for Different Initial Pressures, Journal of Energy, vol. 75 Number 1 (2026), 9–17
https://doi.org/10.37798/2026751726

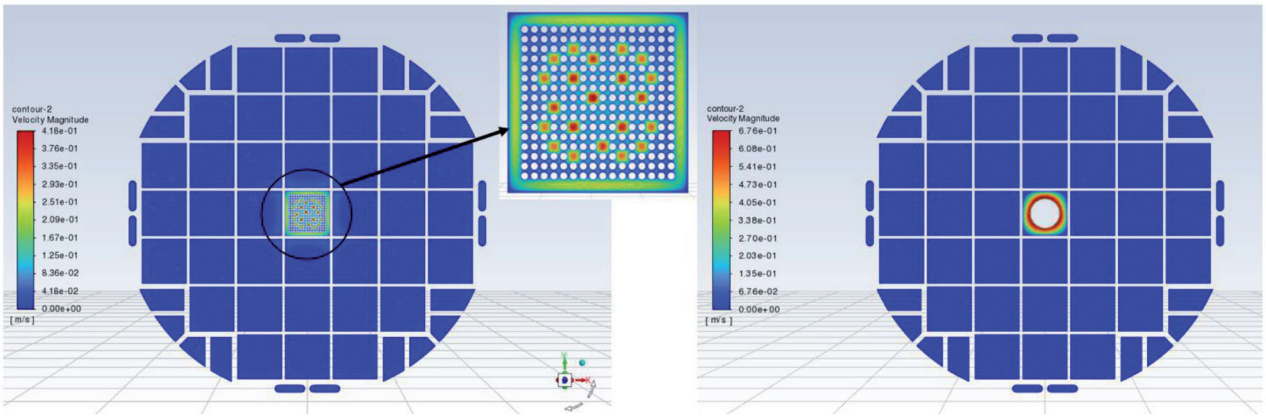

a) Explicit model b) Equivalent model

Fig. 9. Flow velocity distribution at height of 2 m for a) explicit model, and b) equivalent model

B. Different heat source distribution

In this section, we compare results for different heat source distributions and all storage cells populated with equivalent FAs. Uniform and non-uniform power distributions are considered. Uniform distribution means that fuel assemblies have equal heat source intensity. Non-uniform distribution means that each fuel assemblies has its own (real) heat source intensity. In both cases the total heat source is 22.17 kW. For the uniform distribution it means that each fuel assembly releases 599 W of thermal power.

Figure 10 and Figure 11 show radial temperature distribution (local scaling) at height of 2 m and at the top of the MPC. Non-uniform temperature distribution is clearly indicated on the former, however from the latter it is obvious that the temperature distribution at the top of the MPC is almost equal in both cases. Therefore, non-uniform source distribution has no significant influence on the temperature distribution at the top of the MPC and simplified averaged heat source distribution can be used.

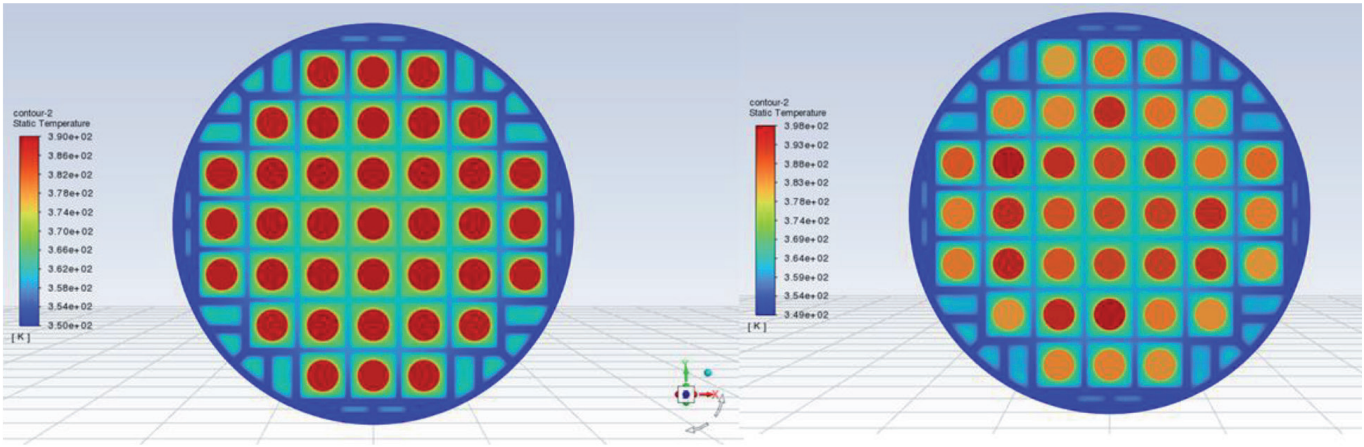

a) Uniform b) Non-uniform

Fig. 10, Radial temperature distribution at 2 m a) uniform, and b) non-uniform FA powers

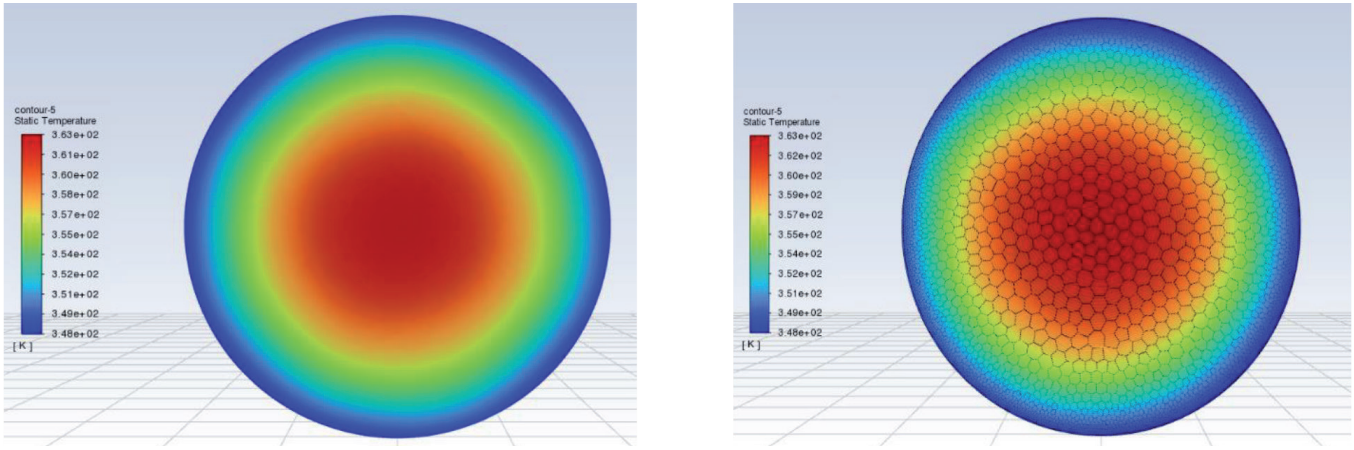

a) Uniform b) Non-uniform

Fig. 11. Local temperature distribution at the MPC top lid a) uniform, and b) non-uniform FA powers

Davor Grgić, Nikola Novosel, Paulina Družijanić, Petra Strmečki, Natural Heat Transfer Performance of Helium Filled Spent Fuel Multi Purpose Container Calculated for Different Initial Pressures, Journal of Energy, vol. 75 Number 1 (2026), 9–17
https://doi.org/10.37798/2026751726

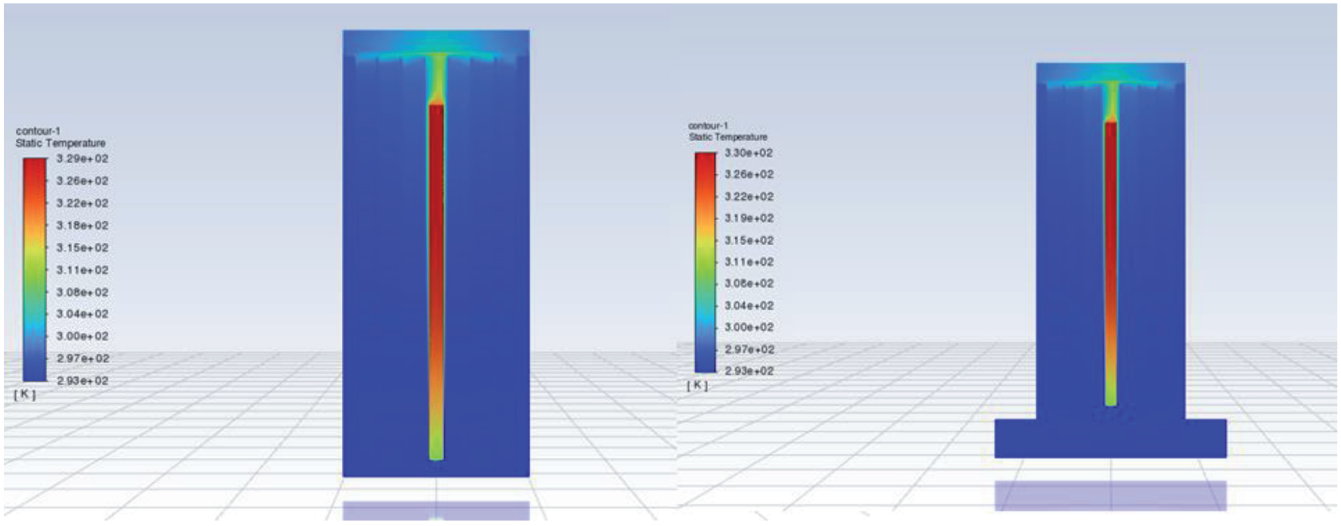

a) Uniform b) Non-uniform

Fig. 12. Temperature distribution a) without a base, and b) with a concrete base

C. Influence of Concrete Base

When placed in a cask, MPC will be at the HI-STORM concrete base. Therefore, a model with concrete base was developed to investigate its influence (reduced bottom heat transfer) on the temperature distribution. The base is 0.5 m thick, and the bottom is fixed at 293 K, while the side is insulated. Convective heat transfer coefficient of 10 W/(m^{2}K) is assumed for the side of the MPC and of 5 W/(m^{2}K) for the top of MPC and the concrete base. The simulation is done for a single equivalent fuel assembly. Temperature distributi-on is shown in Figure 12. The maximum temperature without a base is 329 K, and with a concrete base it is 330 K. The temperature distribution is equal and there is no influence on the maximum FA temperature, but there are differences in the transferred heat in the upper and lower part (lower transfer in lower part when temperatu-re is specified at concrete base bottom).

D. Influence of Aluminium Inserts

The basket is supported against MPC wall with aluminium inserts. Their influence on the temperature distribution is presented in this section. Radial temperature distribution (local scaling) at a height of 2 m is shown in Figure 13. The maximum temperature without inserts is 418 K, and with inserts 404 K. Lower helium temperature is observed for the model with inserts because more heat is removed by conduction through the inserts. Due to the higher thermal conductivity of aluminium than helium, the maximum temperature is lower in the model with inserts. Figure 14 shows the temperature distribution on the MPC surface. The maximum temperature is reached at the top of the MPC and it is 393 K when there are no inserts and 374 K with inserts. It can be observed that a larger area of high temperatures on the MPC mantle is observed in the case with inserts due to the high thermal conductivity of aluminium inserts. Helium flow velocity is shown in Figure 15. A larger region of higher peripheral flow velocities is observed in the case without inserts because more heat is removed by convection. The maximum absolute gas velocity is obtained in case with inserts due to smaller flow cross section area.

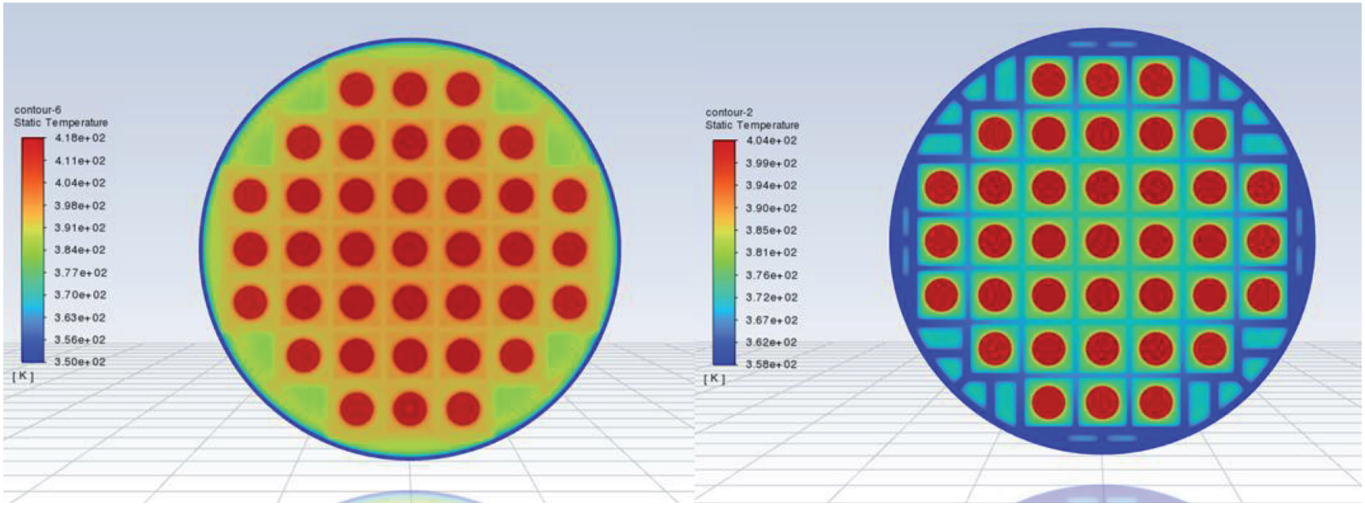

a) Without inserts b) With inserts

Fig. 13. Radial temperature distribution at height of 2 m a) without inserts, and b) with inserts

Davor Grgić, Nikola Novosel, Paulina Družijanić, Petra Strmečki, Natural Heat Transfer Performance of Helium Filled Spent Fuel Multi Purpose Container Calculated for Different Initial Pressures, Journal of Energy, vol. 75 Number 1 (2026), 9–17
https://doi.org/10.37798/2026751726

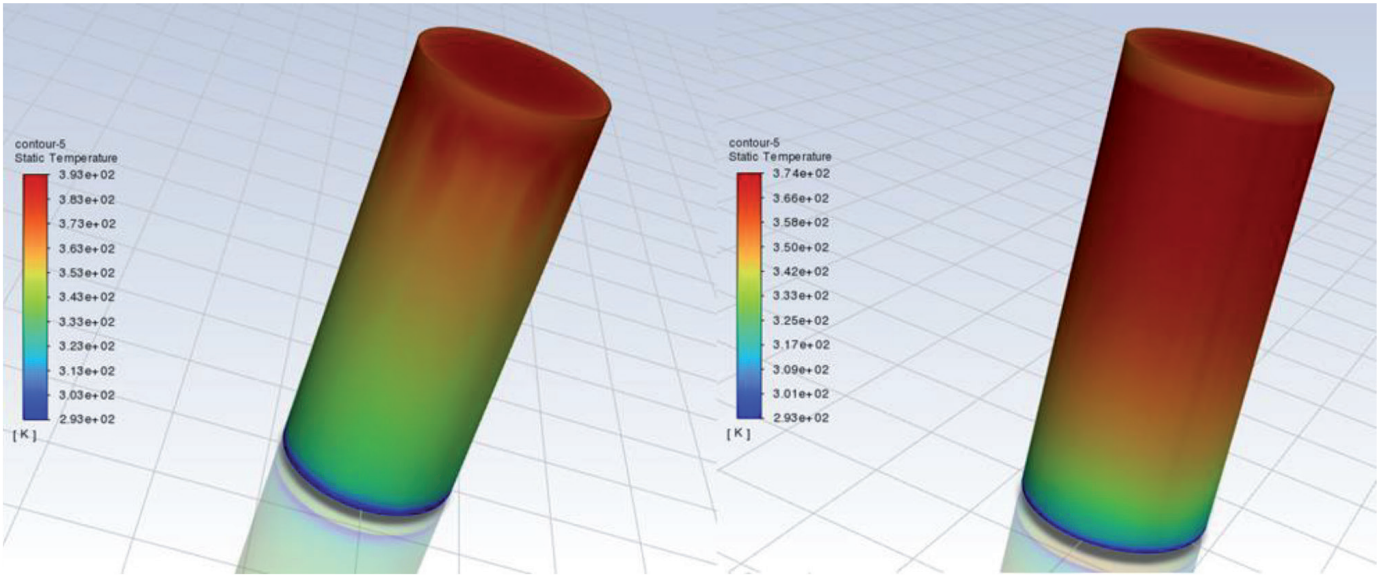

a) Without inserts b) With inserts

Fig. 14. Temperature distribution on the surface of the MPC a) without inserts, and b) with inserts

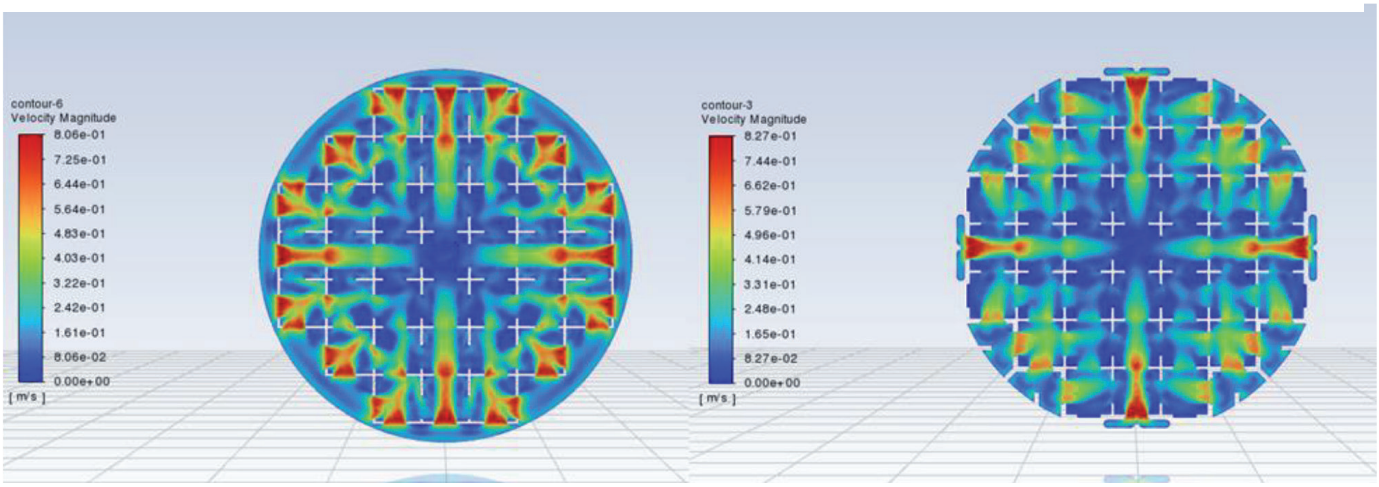

a) Without inserts b) With inserts

Fig. 15. Helium flow velocity at height of 0.05 m a) without inserts, and b) with inserts

E. Different Fill Pressure

The reference pressure in MPC is 4 bars and the limiting pressure is 8 bars, therefore in this section we provide results for different helium fill pressures, ie. the reference pressure, the limiting pressure and one value in between the two (6 bars). Radial temperature distribution (local scaling) at height of 2 m for the pressure of 4, 6, and 8 bars is shown in Figure 16. The maximum tempera-tures at 4, 6 and 8 bars are 404 K, 394 K, and 386 K, respectively. It can be observed that the temperature distribution is similar in all cases. Figure 17 shows temperature distribution on the surface of the MPC. The maximum temperatures are 374 K for 4 bars, 372 K for 6 bars, and 371 for 8 bars. As the pressure increases, both the maximum fuel temperature (to a greater extent) and the maximum temperature on the outer surface of the MPC (to a lesser extent) decrease. The higher the pressure, the more efficient the cooling is. Helium velocity is shown in Figure 18. Lower maximum flow velocity is observed at higher pressure due to smaller temperature difference and larger density (mass) of helium present.

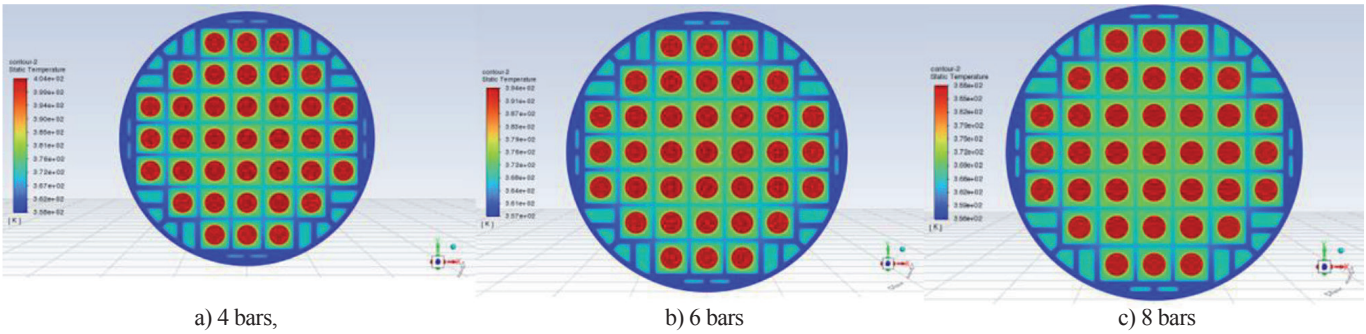

a) 4 bars, b) 6 bars c) 8 bars

Fig. 16. Radial temperature distribution at height of 2 m for the pressure of a) 4 bars, b) 6 bars, and c) 8 bars

Davor Grgić, Nikola Novosel, Paulina Družijanić, Petra Strmečki, Natural Heat Transfer Performance of Helium Filled Spent Fuel Multi Purpose Container Calculated for Different Initial Pressures, Journal of Energy, vol. 75 Number 1 (2026), 9–17
https://doi.org/10.37798/2026751726

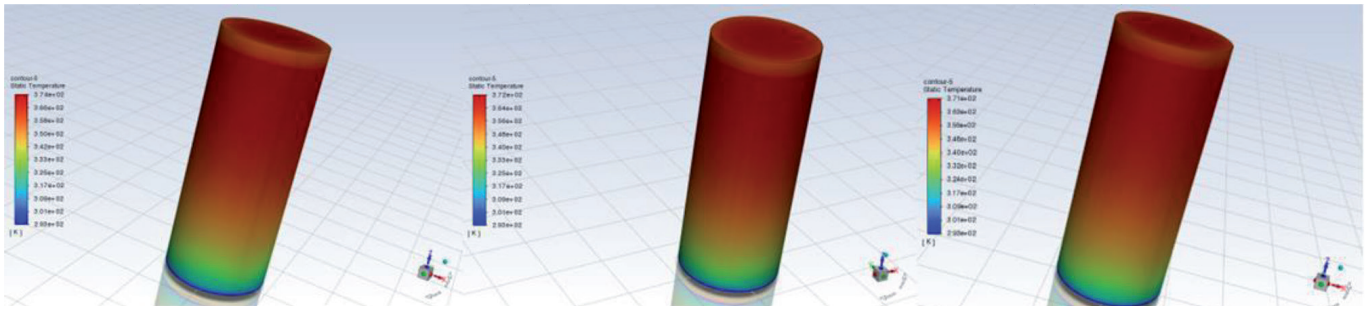

a) 4 bars, b) 6 bars c) 8 bars

Fig. 17. Temperature distribution on the surface of the MPC a) 4 bars, b) 6 bars, and c) 8 bars

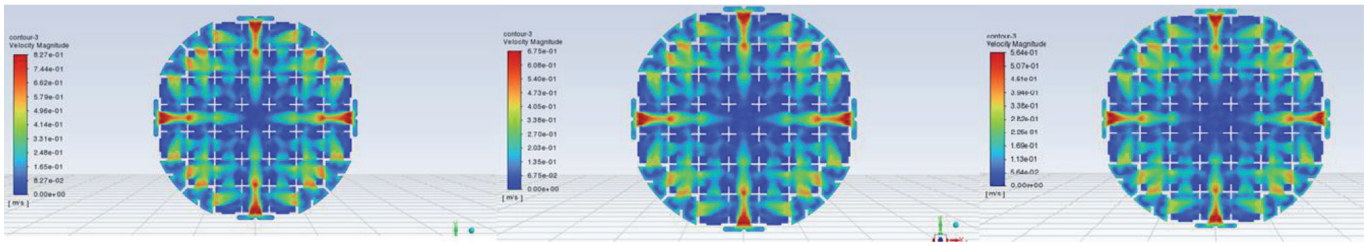

a) 4 bars, b) 6 bars c) 8 bars

Fig. 18. Helium flow velocity at height of 0.05 m for the pressure of a) 4 bars, b) 6 bars, and c) 8 bars

G. Different Cooling Medium

Lastly, we investigated the influence of the cooling medium heat transfer properties on the temperature distribution. In case of long-term helium leakage, air would partially fill the MPC. These two gases differ in thermal conductivity (0.0242 W/(m•K) for the air, and 0.152 W/(m•K) for helium). In this case, the model with concrete base and 37 equivalent fuel assemblies is used. Radial temperature distribution (local scaling) at height of 2 m for helium and air as a cooling medium is shown in Figure 19. The maximum tempera-ture is 429 K for helium and 440 K for the air.

Figure 20. shows the temperature distribution at the top of the MPC. The maximum temperature for helium case is 387 K, and for air 370 K. The aver-age temperature for helium is 375.6 K, and for air 364.7 K. Fuel temperatures are higher with air as cooling medium, and the outer surface of the MPC is consequently at a lower temperature due to poorer thermal conductivity of the air than helium. That means that loosing helium means lower cooling efficiency of the fuel assem-blies and their higher temperature. In the same time thermal con-nection between MPC basket and MPC surface is better with heli-um than with air. Flow velocity is shown in Figure 21. Higher velocities are observed in case of helium cooling.

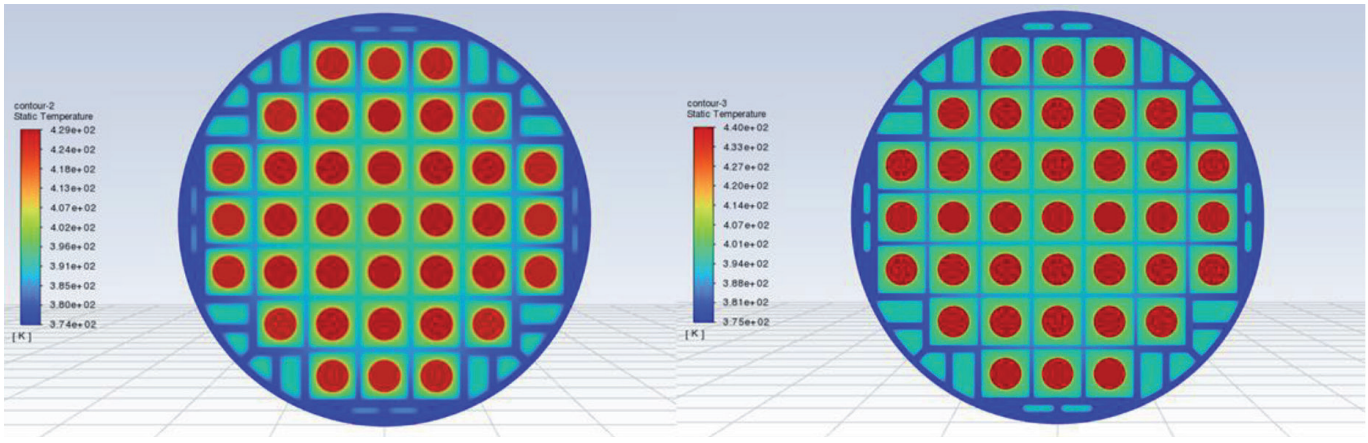

a) helium b) air

Fig. 19. Radial temperature distribution at height of 2 m with a cooling medium a) helium, b) air

Davor Grgić, Nikola Novosel, Paulina Družijanić, Petra Strmečki, Natural Heat Transfer Performance of Helium Filled Spent Fuel Multi Purpose Container Calculated for Different Initial Pressures, Journal of Energy, vol. 75 Number 1 (2026), 9–17
https://doi.org/10.37798/2026751726

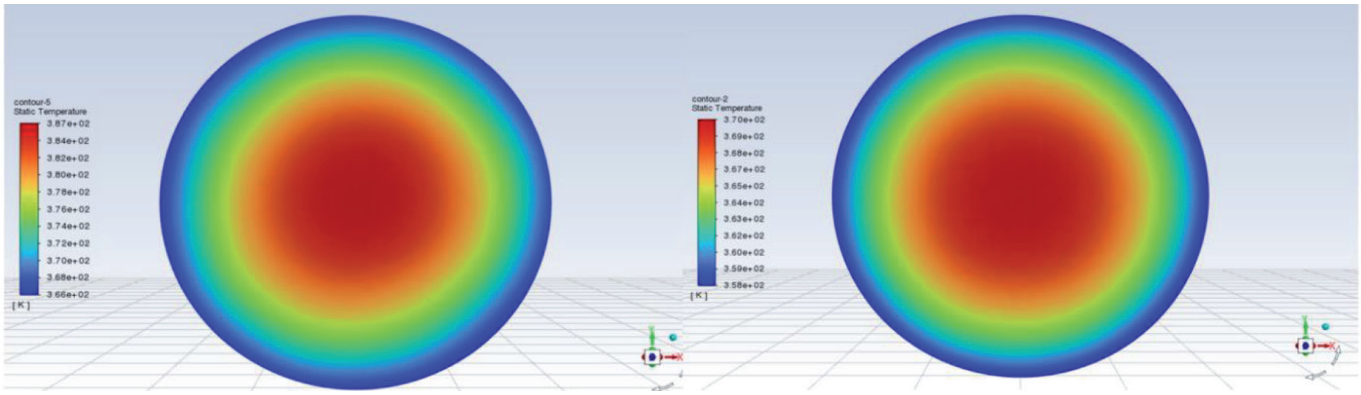

a) helium b) air

Fig. 20. Temperature distribution at the MPC top lid surface with a cooling medium a) helium, b) air

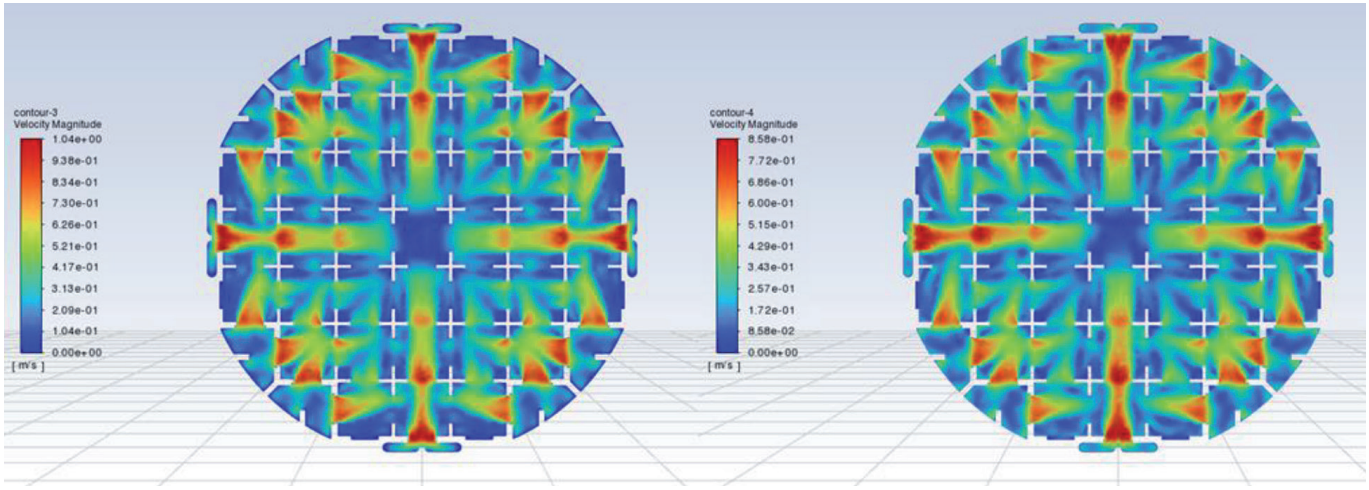

a) helium b) air

Fig. 21. Flow velocity at height of 0.05 with a cooling medium a) helium, b) air

IV Conclusion

This work presents a thermal analysis of simple model of helium filled Holtec's MPC with 37 spent fuel assemblies. The calculations were performed using the Ansys Fluent code in steady state. The explicit and equivalent modes are developed. The equivalent model of the fuel assembly has shown to be good enough if we are not interested in the temperature distribution of the fuel element itself. The uniform and non-uniform heat source distribution was also investigated. It was demonstrated that the non-uniform distribution of the heat source does not have a big impact on the temperature distribution on the outer surface of the MPC. Furthermore, a concrete base had no influence on the temperature distribution, but there were differences in heat transferred in the upper and lower part of the MPC. The influence of inserts on temperature distribution showed that more efficient cooling was achieved with inserts due to the higher thermal conductivity of aluminium than helium. The analysis of the influence of the initial fill pressure showed more efficient cooling at a higher pressure, as expected. Finally, the analysis of different cooling medium demonstrated more efficient cooling with helium compared to air. Additional analyses will be needed to determine the relation between the temperature difference and helium to air fraction in the MPC gas.

References

[1] Holtec International, Final safety analysis report on the HI-STORM FW system, HI-2114830

[2] Holtec International. *Thermal Evaluation Of Loaded MPC-37 With Krsko's Design Basis Heat Load In HI-STORM FW System Under All Duct Blockage Accident*. USA, 2018.

[3] J. Penalva, F. Feria, L.E. Herranz; Thermal performance of a concrete cask: Methodology to model helium leakage from the steel canister

[4] Ansys Academic Research Mechanical, Release 2020R2, Help System, Coupled Field Analysis Guide, Ansys, Inc.

[5] NPP Krško USAR rev. 29 Chapter 21, Krško 2023

[6] Nuclear Regulatory Commission; Computational Fluid Dynamics Best Practice Guidelines for Dry Cask Applications

Davor Grgić, Nikola Novosel, Paulina Družijanić, Petra Strmečki, Natural Heat Transfer Performance of Helium Filled Spent Fuel Multi Purpose Container Calculated for Different Initial Pressures, Journal of Energy, vol. 75 Number 1 (2026), 9–17
https://doi.org/10.37798/2026751726

Scientific paper
Manuscript received February 6, 2026; revised March 6, 2026; accepted March 13, 2026

Journal of Energy

VOLUME 75 Number 1 | 2026

journal homepage: http://journalofenergy.com/

Development and Validation of Dynamic RMS Models for Power System Analysis

Petar Vinković, Renata Rubeša, Goran Levačić

***Summary* — The increasing integration of converter-based renewable energy sources is reducing the inertia of power systems and amplifying transient oscillations following disturbances. As a result, the accuracy of dynamic simulation models of generating units has become essential for reliable assessment of system transient stability. This paper presents a validation procedure for a root-mean-square dynamic model of Unit D of the Zakucacˇ hydropower plant, based on measurements obtained from a phasor measurement unit during and after a real system disturbance. The validation process includes preparation of measurement data, alignment of the static model with steady-state measurements, and detailed tuning of dynamic model parameters. The achieved results demonstrate a high level of agreement between simulated and measured responses. In addition, the paper highlights the importance of standardizing requirements for the submission of simulation models, as accurate modeling of individual generating facilities directly enhances the credibility of system-level analyses and supports secure and stable power system operation under increasing system complexity.**

***Keywords* — dynamic model, RMS model, validation, PMU**

I. Introduction

In April 2025, a massive power outage occurred on the Iberian Peninsula, representing the largest energy-related incident in Europe over the past decade. Although the causes of such events are often multiple, public criticism has increasingly been directed toward renewable energy sources (RES) and the ongoing energy transition. These concerns are not entirely unfounded, as the integration of RES, while essential for decarbonization, often displaces conventional generating units, resulting in a reduction of the overall inertia of the power system.

System inertia plays a crucial role in maintaining frequency stability by providing an immediate and inherent response of synchronous generators to active power imbalances. As system inertia decreases, the power system becomes more vulnerable to disturbances. In particular, following a major generation outage, the rate of change of frequency increases, the frequency nadir occurs earlier, and the depth of the frequency deviation becomes more pronounced, significantlyreducing the system's resilience to disturbance and increasing the risk of cascading outages triggered by protection systems.

In order to prevent such incidents, it is essential to identify potential stability issues in advance. This is only possible if the mathematical models used in system studies accurately represent the actual system behavior. In this context, model validation is of utmost importance, as it confirms the reliability and applicability of models used in stability analyses.

The first part of this paper presents a dynamic model validation procedure based on a single generating unit of the Zakucac hydropower plant. The second part emphasizesˇ the need to establish clear guidelines for the submission of dynamic models by generating units connecting to the power system.

II. Dynamic Model Validation

A. Role of Dynamic Models in Power System Studies

Mathematical models are used for the design, operation, and planning of power systems to describe the behavior of generating units, network components, and the system as a whole. Of particular importance are dynamic models, which enable the analysis of time-varying phenomena such as system response to disturbances, oscillations, voltage stability, and rotor angle stability.

In accordance with Commission Regulation (EU) 2017/1485 establishing guidelines on electricity system operation, commonly referred to as the System Operation Guidelines (SO GL), transmission system operators (TSOs) are explicitly required to assess the dynamic stability of the power system as part of continuous system operation and security planning. Dynamic stability refers to the ability of the power system to remain in a balanced and synchronized state following major disturbances, such as short circuits, sudden loss of generation, large load variations, or the operation of protection systems.

In practice, two main types of dynamic models are used. RMS models simplify simulations by considering only the root-mean-square values of voltages, currents, and powers, assuming quasi-stationary behavior. EMT (Electromagnetic Transient) models, on the other hand, enable detailed analysis of fast electromagnetic phenomena in the time domain, including high-frequency components with time resolutions on the order of microseconds.

Corresponding author: Petar Vinković
Petar Vinković, Renata Rubeša and Goran Levačić are with the Croatian Transmission System Operator, Zagreb, Croatia (emails: petar.vinkovic@hops.hr; renata.rubesa@hops.hr; goran.levacic@hops.hr)

Petar Vinković, Renata Rubeša, Goran Levačić, Development and Validation of Dynamic RMS Models for Power System Analysis, Journal of Energy, vol. 75 Number 1 (2026), 18–23
https://doi.org/10.37798/2026751740

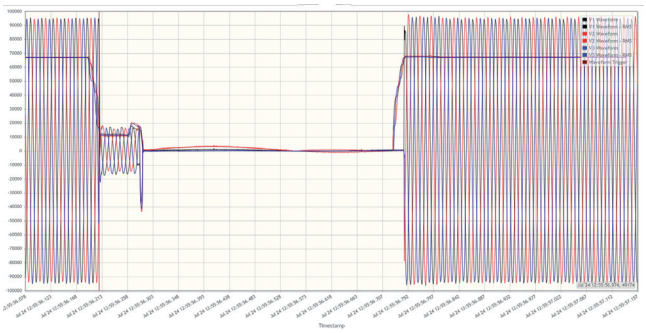

Fig. 1. Three-Phase Short Circuit on TL Jelinak - Glunca˘

Fig. 2. Simulation Model Diagram

Although EMT models provide higher accuracy, especially in converter-dominated networks, their computational complexity and long simulation times limit their applicability in operational and planning studies of large-scale systems. Consequently, RMS models are widely used in operational planning, stability analysis, and grid connection studies, as they offer an acceptable trade-off between accuracy and computational efficiency.

This paper focuses on the development and validation of an RMS dynamic model of a generating unit based on real measurements obtained from a phasor measurement unit (PMU). Such validated RMS models form the foundation for reliable analysis of system behavior during and after disturbances and support informed operational and planning decisions.

B. Recorded Disturbance in the Croatian Power System

In July 2024, a three-phase short circuit was recorded on a 110 kV transmission line (TL) between the Jelinak and Glunca substations. Figure 1 shows the voltage waveforms˘ before, during and after the fault from the COMTRADE file. The estimated fault duration until protection operation was approximately 80 ms, after which the line was disconnected. Approximately 460 ms after disconnection, a successful automatic reclosing occurred. This event resulted in deviations of system frequency and voltage, which were particularly pronounced at electrically closer substations.

One of the substations where the disturbance was clearly observed was the Zakucac hydropower plant. During the inci-˘ dent, only one of the four generators was in operation, namely Unit D, which is connected to the 110 kV busbar via a block transformer. This configuration enabled isolated observation of the response of a single generating unit, representing an ideal case for precise dynamic model validation. The diagram of the simulation model is illustrated in Figure 2.

Accordingly, the validation presented in this paper is carried out using the example of Unit D of the Zakucac hydropower˘ plant, demonstrating the model's ability to accurately reproduce the system response during and after the disturbance.

C. Dynamic Model Validation Procedure

A prerequisite for dynamic model validation is the availability of PMU measurements, which serve as the primary data source for validation. PMUs enable synchronized recording of generator responses, providing a reliable basis for comparing simulated and measured responses. In other words, validation is only possible if the generating unit response during and after a disturbance has been captured by PMU measurements. The measurement resolution used in this study was 20 ms, corresponding to a reporting rate of 50 frames per second in a 50 Hz system, which represents a standard configuration in accordance with IEEE C37.118.1 [1]. It should be emphasized that this value represents the reporting interval of synchrophasor estimates rather than the internal signal sampling frequency of the PMU. For RMS dynamic validation focused on electromechanical phenomena, a 20 ms reporting interval provides sufficient temporal resolution. PMU phasor estimation algorithms typically employ window-based signal processing, and a small measurement delay may be present. Therefore, the measurement and simulation signals were timealigned prior to comparison.

The dynamic model validation process can be divided into three main steps:

1. **Preparation of measurement data:** The first step involves processing PMU data. The quantities of interest include RMS values of the active and reactive power of the generating unit, as well as frequency and voltage magnitude at the high-voltage busbar.
2. **Static model alignment:** Prior to dynamic model validation, the steady-state power flow must be properly aligned with the measured operating point. Accordingly, the simulated pre-disturbance active and reactive power outputs should closely match the measured values.
3. **Dynamic model validation:** The key validation step involves comparing the simulated dynamic response with the measured response during the disturbance. Model parameters are tuned to achieve the best possible agreement with measurements.

The steady-state parameters of the generator and the associated block transformer used in the simulation model are summarized in Tables I and II. Simulations were performed using the PSS®E software tool (Siemens PTI). The parameter notation follows the conventions used in the PSS®E environment. Figures 3 and 4 show the implementation of these parameters in the PSS®E environment. These parameters define the steady-state operating point used as the initial condition for the dynamic simulations.

The dynamic model of the generating unit includes the generator model, excitation system, turbine governor, power system stabilizer, and voltage measurement compensation model.

Although leading technical organizations such as IEEE, NERC, ENTSO-E, and CIGRE do not prescribe strict numeri-´ cal acceptance criteria for validated models [2]–[5], a set of engineering principles has been established in practice to assess model adequacy. Model quality is typically evaluated through both quantitative and qualitative comparison of simulated and measured responses under real disturbance conditions. model adequacy. Model quality is typically evaluated through both quantitative and qualitative comparison of simulated and measured responses under real disturbance conditions.

Petar Vinković, Renata Rubeša, Goran Levačić, Development and Validation of Dynamic RMS Models for Power System Analysis, Journal of Energy, vol. 75 Number 1 (2026), 18–23
https://doi.org/10.37798/2026751740

TABLE I
GENERATOR STEADY-STATE PARAMETERS

Parameter	PSS®E	Value	Unit
Rated apparent power S_n	MBASE	160	MVA
Rated voltage (generator bus)	BASKV	16	kV
Maximum active power P_{max}	PMAX	144	MW
Minimum active power P_{min}	PMIN	63	MW
Maximum reactive power at P_{max}	QMAX	69.7	MVAr
Minimum reactive power at P_{max}	QMIN	-19.4	MVAr
Source impedance (real part)	RSOURCE	0	p.u.
Source impedance (imaginary part)	XSOURCE	0.2068	p.u.
Scheduled voltage	VSCHED	1.01	p.u.

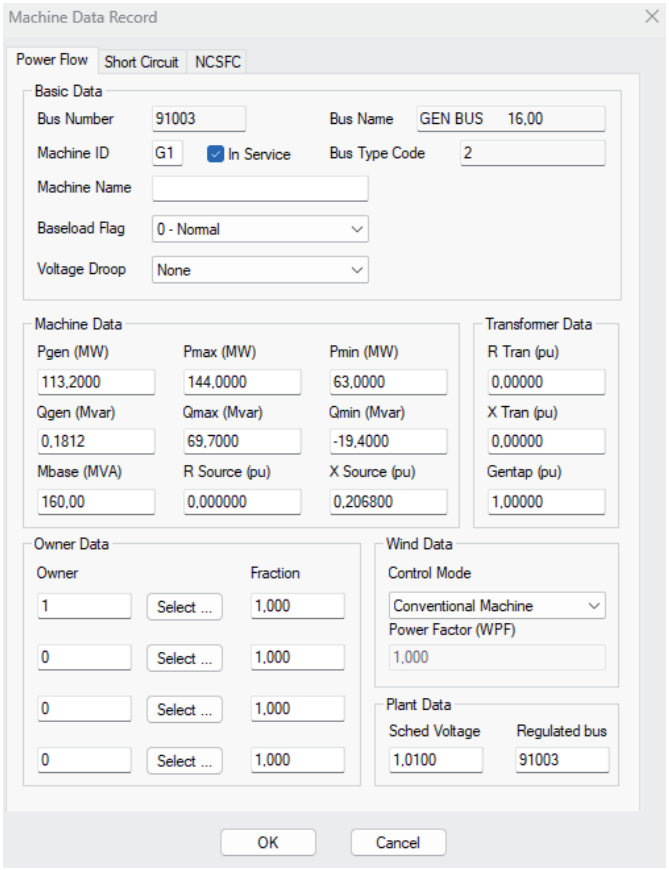

Fig. 3. Machine Data for Power Flow Analysis

TABLE II
BLOCK TRANSFORMER PARAMETERS

Parameter	PSS®E	Value	Unit
Rated apparent power S_n	Winding MVA	160	MVA
Rated voltage (HV side)	Winding 1 Nominal	121	kV
Rated voltage (LV side)	Winding 2 Nominal	16	kV
Tap setting voltage	Winding 1 Voltage	114.95	kV
Vector group	Vector Group	YNd5	–
Number of tap positions	Tap positions	7	–
Upper tap limit	R1max	1.155	p.u.
Lower tap limit	R1min	0.99	p.u.
Short-circuit (SC) losses	Load loss	510000	W
SC impedance magnitude	Z	0.131	p.u.
No-load losses	No load loss	60000	W
Magnetizing current	I0	0.00111	p.u.

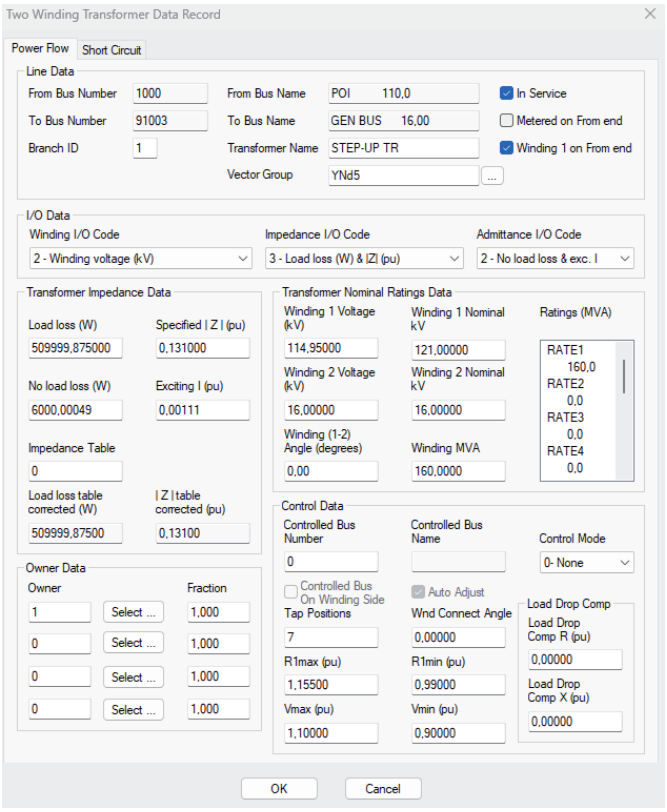

Fig. 4. Transformer Data for Power Flow Analysis

In this context, an acceptable model should satisfy the following criteria: good agreement in key variables such asactive and reactive power, frequency, and bus voltage; acceptable deviations in amplitude and timing; consistency across different disturbance scenarios; numerical stability; and final acceptance based on engineering judgment considering the intended application of the model.

D. VALIDATION RESULTS

After all validation steps were completed, the response of the generating unit was simulated to the recorded frequency deviation and voltage dip. For this purpose, a playback model available in the PSS®E software package was used. The playback model allows measured time series signals, in this case the RMS voltage and frequency recorded by the PMU on the 110 kV busbar of the Zakucac hydropower plant, to be˘ injected directly into the dynamic simulation.

These signals are reproduced as time-varying inputs, enabling the simulated model to respond to the same excitation as the actual generating unit experienced during the disturbance. This approach eliminates the need to model the remainder of the network or the conditions that caused the disturbance and allows the analysis to focus exclusively on the response of the generating unit.

Figure 5 shows the RMS voltage value from the PMU at the point of interconnection (POI), while Figure 6 shows the frequency from the PMU at the same point. Figure 7 compares the voltage from PMU measurements with the voltage used as input to the simulation. Figure 8 compares the frequency from PMU measurements with the frequency used as input to the simulation. Figures 7 and 8 show how the playback model faithfully reflects the recorded measurement data in the simulation environment.

Petar Vinković, Renata Rubeša, Goran Levačić, Development and Validation of Dynamic RMS Models for Power System Analysis, Journal of Energy, vol. 75 Number 1 (2026), 18–23
https://doi.org/10.37798/2026751740

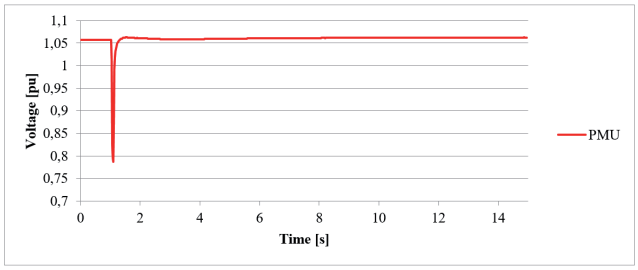

Fig. 5. RMS Voltage Value from PMU

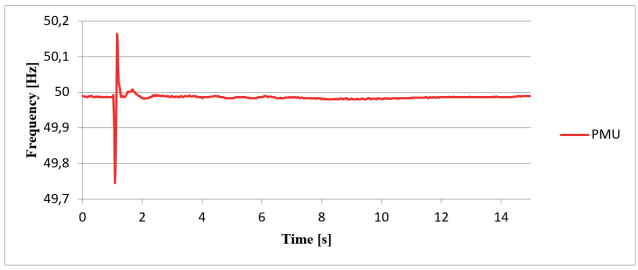

Fig. 6. Frequency Value from PMU

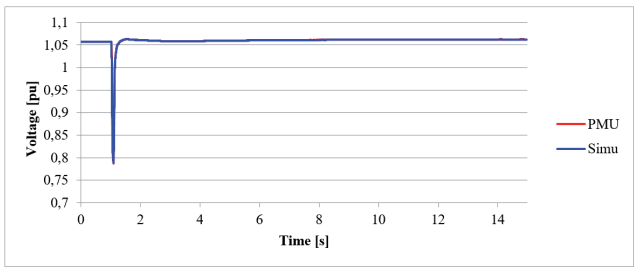

Fig. 7. Comparison of Voltage PMU Measurement and Simulation Input

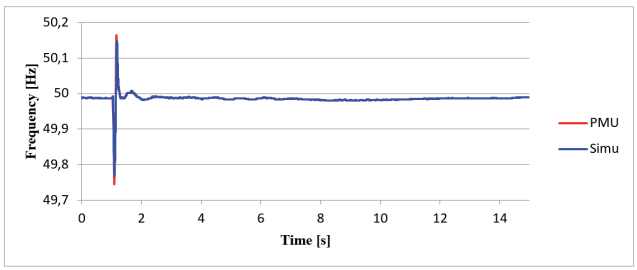

Fig. 8. Comparison of Frequency PMU Measurement and Simulation Input

Initial simulations revealed discrepancies in active and reactive power responses, indicating that the initial dynamic model did not sufficiently represent the actual unit behavior, as can be seen in Figure 9 and Figure 10. Therefore, parameter tuning was performed, including adjustments for inertia, time constants, reactances, excitation system parameters, and voltage measurement compensation.

Following tuning, very good agreement between the measured and simulated responses was achieved (Figure 11 and Figure 12), particularly during the first few seconds after the disturbance, which is critical for transient stability assessment. Remaining discrepancies in reactive power during the settling into a new steady-state indicated the need to include a reactive power regulator (Q-regulator) in the model.

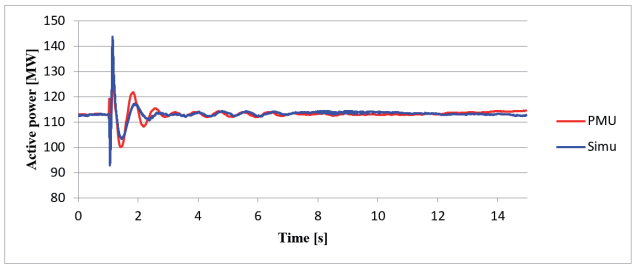

Fig. 9. Comparison of Measured and Simulated Active Power Response

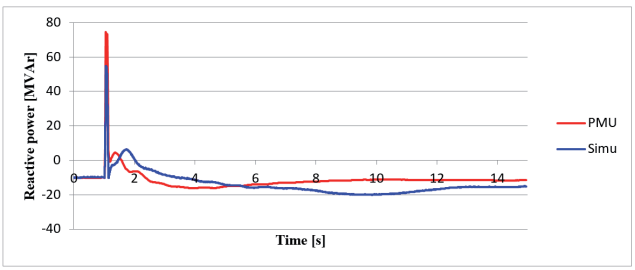

Fig. 10. Comparison of Measured and Simulated Reactive Power Response

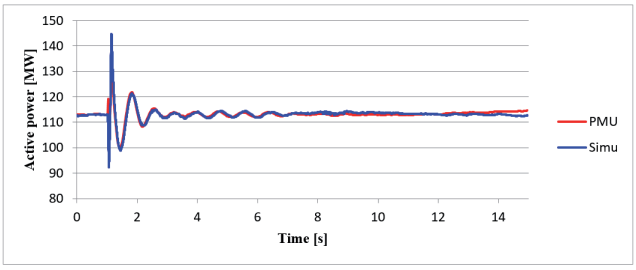

Fig. 11. Comparison of Measured and Simulated Active Power Response

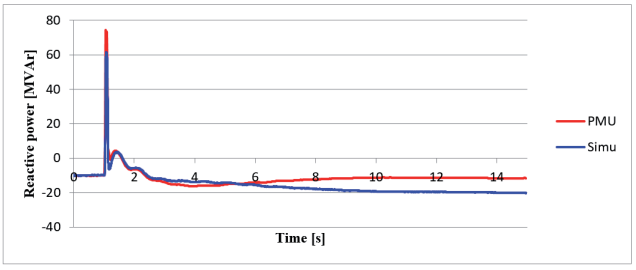

Fig. 12. Comparison of Measured and Simulated Reactive Power Response

The Q-regulator acts as a supervisory control over the excitation system, restoring reactive power output to its predisturbance reference value. As can be seen in Figure 13 and Figure 14, after incorporating and properly tuning the Qregulator, the reactive power response showed good agreement with measured data, resulting in an overall acceptable model validation.

E. Further Steps

The validation of the dynamic model of Unit D of the Zakucac hydropower plant represents only the first step in˘ a broader process of establishing systematically validated generating unit models within the Croatian power system. Following the successful validation of this unit, the logical next step is to extend validation activities to other generating facilities. It is important to emphasize that the validated model should also be examined under different types

Petar Vinković, Renata Rubeša, Goran Levačić, Development and Validation of Dynamic RMS Models for Power System Analysis, Journal of Energy, vol. 75 Number 1 (2026), 18–23
https://doi.org/10.37798/2026751740

of disturbances, as validation against a wider range of operating conditions and events contributes to increased model robustness and confidence in its dynamic performance.

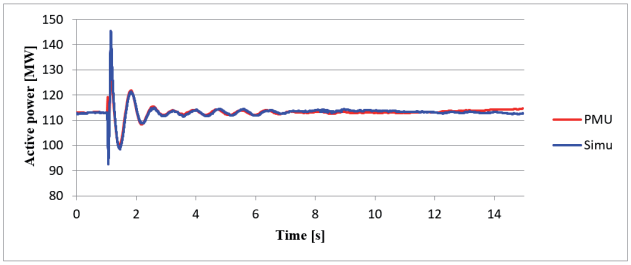

Fig. 13. Comparison of Measured and Simulated Active Power Response

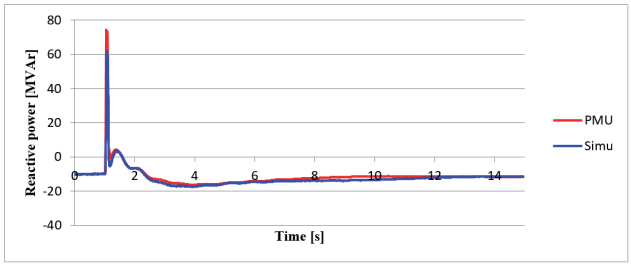

Fig. 14. Comparison of Measured and Simulated Reactive Power Response

A key prerequisite for successful validation is the availability of high-quality, time-synchronized measurement data. In this regard, the PMU coverage of the Croatian transmission system is at a high level and continues to improve. Expanding validation efforts, together with the development of standardized model submission requirements, will significantly enhance the reliability of dynamic studies and support secure power system operation under increasing shares of RES.

III. Submission of RMS Simulation Models of Generating Plants

The validation of simulation models of currently connected generating plants represents the basis for the final verification of the overall power system model. However, due to the continuous inflow of new connection requests for generating facilities, and in order to avoid retroactive model validation, the Croatian Transmission System Operator (HOPS) has initiated the development of a document defining the requirements for the submission of static and dynamic RMS models of generating plants.

The static and dynamic models together form a simulation model. The document will define guidelines for the submission and validation of simulation models of power park modules connecting to the transmission network of the Republic of Croatia. The defined guidelines will apply to conventional power plants, wind power plants (type III and type IV), solar photovoltaic power plants, and battery energy storage systems.

According to Article 81 of the Transmission System Network Code, the transmission system operator (TSO) must have accurate knowledge of the dynamic behavior of connected plants, as well as those intended to be connected to the transmission network. Upon request by the TSO, the transmission network user is obliged to provide the required data and technical documentation related to its facility [6]. Considering the increasing penetration of RES-based generating units and the associated reduction of overall system inertia, dynamic analysis of the behavior of multiple generating facilities has become essential for a reliable assessment of power system stability. Understanding the mutual interaction of these units is crucial for preventing disturbances and maintaining frequency stability under conditions of system transition.

The guidelines will be aligned with the recommendations of the Western Electricity Coordinating Council (WECC) regarding the submission of second-generation generic models [7]. Generic models enable manufacturers to represent their equipment without disclosing proprietary information to other users.

In the first phase, the simulation model would be submitted a specified number of days prior to the planned connection of the facility to the network. This initial model must include all key components: the generator model, excitation system, turbine governor, power system stabilizer (if applicable), and, where necessary, compensation and supervisory control loops. Along with the model itself, technical documentation must be provided, including a list of the generic models used, numerical values of all parameters, and a description of their origin. After connection to the network, an updated simulation model must be resubmitted, including possible corrections of parameters of the previously submitted static or dynamic model. Corrections may arise from the final selection of control equipment, observed differences in system responses, or the execution of commissioning tests. In this phase, the simulation model is submitted together with the final verification test report.

The submitted simulation model will be validated against field measurements obtained through the Operational Test Plan and Program of the generating facility. The validation procedure would follow the same methodology as presented earlier in this paper. Specifically, voltage and angle (frequency) measurements at the POI would be recorded and reproduced in the simulation, after which the active and reactive power responses obtained from the simulation model would be compared with field measurements.

The document would define requirements regarding the accuracy of simulated and measured responses, based on which the submitted simulation model would be deemed acceptable or unacceptable.

This consideration is currently limited to RMS models; however, trends indicate that transmission system operators are increasingly requiring the submission of EMT models as well, particularly for converter-based grid users. EMT models extend the conventional classification of power system stability (angle, frequency, and voltage stability) to include resonance stability and converter-driven stability. A prerequisite for diagnosing “hidden issues” such as resonance is the accuracy and quality of the available data. Operators in Australia (AEMO) and the United Kingdom (NGESO) are examples where users are required to submit EMT models [8], [9]. In the forthcoming period, the need to require EMT models will be considered in order to perform more detailed analyses of interactions and the impact of new users on the network.

IV. Conclusion

With the increasing integration of converter-based RES, the inertia of the power system is decreasing, while oscillations of transient phenomena following disturbances are becoming larger and more pronounced. In this context, the accuracy of simulation models of generating units becomes crucial for the assessment of system transient stability. This paper presents a validation procedure for the RMS model of Unit D of the Zakucac hydropower plant using data collected by a PMUˇ device during and after a recorded disturbance. The process includes the preparation of measurement data, alignment of the static model with measurements, and precise tuning of dynamic model parameters. The result is a

Petar Vinković, Renata Rubeša, Goran Levačić, Development and Validation of Dynamic RMS Models for Power System Analysis, Journal of Energy, vol. 75 Number 1 (2026), 18–23
https://doi.org/10.37798/2026751740

high level of agreement between simulated and measured responses. Furthermore, the need for standardization of requirements for the submission of simulation models is emphasized. Reliable modeling of individual generating facilities directly contributes to the credibility of system-wide simulations and represents a key tool for preserving the stability and security of power system operation in an increasingly dynamic and complex energy environment.

Acknowledgments

Generative AI tools (ChatGPT, OpenAI, GPT-4) were used solely to improve language clarity and readability.

References

[1] IEEE Power and Energy Society, "IEEE Standard for Synchrophasor Measurements for Power Systems," IEEE Std C37.l18.1-2018, Dec. 2018.

[2] IEEE PES Task Force on Model Validation, "Generator model validation—Applications of PMU measurements," presented at the IEEE PES General Meeting, Pittsburgh, PA, USA, Jul. 2008.

[3] North American Electric Reliability Corporation (NERC), "Reliability Guideline: Power Plant Model Verification and Testing for Synchronous Machines," Atlanta, GA, USA, Jul. 2018. [Online]. Available: https://www.nerc.com/globalassets/who-we-are/standing-committees/rstc/irps/re-liability guideline - ppmv for synchronous machines - 2018-06-29.pdf

[4] ENTSO-E, "Implementation Guidance Document: Compliance Verification – Monitoring after operational notification," Brussels, Belgium, 2021 (updated 2023). [Online]. Available: https://www.entsoe.eu/Documents/Network\%20codes\%20documents/ NC\%20RfG/IGD Compliance Verification –Monitoring after operational notification final for publication.pdf

[5] CIGRE Working Group B5.39, "Application of phasor measurement units for monitoring power system dynamic performance," CIGRE Technical Brochure 702, Paris, France, Feb. 2017.

[6] Hrvatski operator prijenosnog sustava d.d. (HOPS), "Mrezna pravila˘ prijenosnog sustava," Zagreb, Croatia, Dec. 2023. [Online]. Available: https://www.hops.hr

[7] Western Electricity Coordinating Council (WECC), "Guidelines / Modeling Practices," 2025 (ongoing updates). [Online]. Available: https: //www.wecc.org

[8] National Energy System Operator (NGESO), "Grid Code modification GC0141 – EMT Modelling Requirements," 2024. [Online]. Available: https://www.neso.energy/document/275661/download

[9] Australian Energy Market Operator (AEMO), "Power System Model Guidelines 2023," 2023. [Online]. Available: https://aemo.com.au/-/media/files/electricity/nem/security and reliability/ system-security-market-frameworks-review/2023/power systems model guidelines 2023 published .pdf

Petar Vinković, Renata Rubeša, Goran Levačić, Development and Validation of Dynamic RMS Models for Power System Analysis, Journal of Energy, vol. 75 Number 1 (2026), 18–23
https://doi.org/10.37798/2026751740

Scientific paper
Manuscript received January 22, 2026; revised February 28, 2026; accepted March 13, 2026.

Journal of Energy

VOLUME 75 Number 1 | 2026

journal homepage: http://journalofenergy.com/

Smart Hybrid Metaheuristic Model for Enhanced Wind Energy Production

Muhammad Rashid, Syed Mohammad Ali Shah, Abdur Raheem, Saeed Uddin Shaikh, Rabia Shakoor, Zeeshan Ahmad Arfeen

***Summary* — This study presents a hybrid Particle Swarm Optimization–Genetic Algorithm (PSO-GA) technology integrated into a structured three-phase strategy to address the wind farm layout optimization (WFLO) problem. In order to enhance total energy efficiency through intelligent turbine location, the proposed strategy is applied to a particular wind farm scenario. Three case studies, each representing varying degrees of wake and non-wake settings, are analyzed to assess the robustness of this method. In order to prevent severe wake interference, the system finds the best location for turbines while strictly following to industry-standard spacing standards. The suggested hybrid model consistently improves energy extraction and reduces wake losses by 20–28% in all scenarios when compared to current method like PSO-based design by [21]. The hybrid PSO-GA still has a moderate computational cost, taking about 20 seconds each simulation. This is just 10–15% more than standalone PSO, but it produces far greater convergence stability.**

***Keywords* — Hybrid PSO-GA Algorithm; Wind Farm Layout Optimization (WFLO); Wind Turbine Placement**

I. Introduction

The share of renewable energy in global electricity generation has continued to rise, supported by record additions of solar and wind power, as portrayed in Figure 1. According to the Statistical Review of World Energy 2023, solar and wind energy collectively contributed 14% of global electricity generation in 2022. Consequently, the adoption of renewable energy sources continues to gain widespread momentum [1].

The Energy Institute Statistical Review of World Energy 2024 also estimates that in 2023, renewable energy was producing some 30 per cent of the world's electricity, with wind energy generating almost 8 per cent of all electricity in the world [2]. The Global Wind Energy Council (GWEC) Global Wind Report 2024 reveals that total installed wind capacity exceeded 1,020 GW globally in 2023, demonstrating consistent annual growth propelled by offshore and utility-scale installations. These results underscore the growing strategic significance of wind generation in meeting global decarbonization objectives [3, 4].

However, as the number of turbines in a wind farm enhance, the complexity of development grows proportionally with the area required. This has shifted the focus toward minimizing electricity generation costs, optimizing wind farm layouts, and improving the efficient utilization of wind resources.

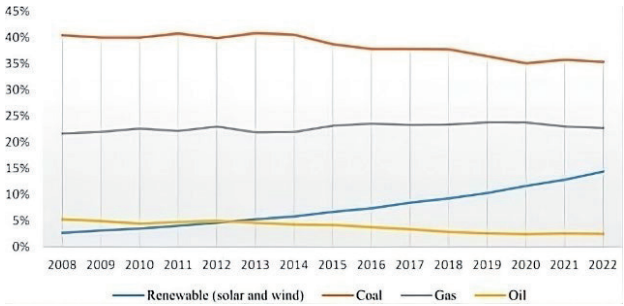

Fig. 1. Share of energy in power by type [1].

The Wind Farm Layout Optimization (WFLO) challenge is inherently nonlinear and constrained, involving multiple interdependent variables. An inefficient arrangement of Wind Turbines (WTs) can adversely affect their operational performance and intensify wake interactions [5]. Accurately simulating wake effects remains one of the most complex and computationally demanding aspects of wind farm optimization. Numerous wind farm layout strategies have been suggested recently to enhance power generation while minimizing wake losses [5].

Frandsen et al. [6] refined the classical Jensen wake framework by considering nonlinear wake boundaries. Subsequent researchers such as Mittal and Mitra [7] adopted the Jensen framework to formulate cost-efficient wind farm layouts, while others [8] have introduced various wake modeling approaches, including Gaussian-based and three-dimensional analytical frameworks. Despite these alternatives, the Jensen framework remains the most widely applied in WFLO due to its simplicity and computational efficiency [9]. In this research, the Jensen wake framework is employed to estimate wake effects, enabling a balance between accuracy and computational cost. Though many metaheuristic optimization strategies have been used for WFLO, the majority of current approaches either just concentrate on maximizing power or are not resistant to changing wind conditions. Furthermore, hybridized evolutionary methods that balance wake interactions, energy production, and computing efficiency have received little attention. Thus, in comparison to

Corresponding author: Muhammad Rashid

Muhammad Rashid, Abdur Raheem, Rabia Shakoor and Zeeshan Ahmad Arfeenare with the The Islamia University of Bahawalpur, Bahawalpur, Pakistan (emails: engr.rashid@iub.edu.pk; abdur.raheem@iub.edu.pk; rabia.shakoor@iub.edu.pk; zeeshan.arfeen@iub.edu.pk)

Syed Mohammad Ali Shah and Saeed Uddin Shaikh are with the Hyderabad Institute for Technology and Management Sciences, Hyderabad, Pakistan (emails: doric@hitms.edu.pk; rector@hitms.edu.pk)

Muhammad Rashid, Syed Mohammad Ali Shah, Abdur Raheem, Saeed Uddin Shaikh, Rabia Shakoor, Zeeshan Ahmad Arfee, Smart Hybrid Metaheuristic Model for Enhanced Wind Energy Production, Journal of Energy, vol. 75 Number 1 (2026), 24–29
https://doi.org/10.37798/2026751739

the state-of-the-art, this study offers a structured hybrid PSO-GA architecture that improves WFLO dependability under three actual wind situations while consistently increasing efficiency and reducing wake loss. The proposed method achieves consistent improvements (0.2% efficiency gain per case) and significantly lowers wake losses compared to the benchmark study in [21].

The hybrid PSO-GA performs well, but it depends on the simplified Jensen model, which might not adequately represent intricate turbulence interactions in offshore or extremely uneven terrain. Performance may change with deeper search parameter customization, and the computational cost rises somewhat with farm size. More advanced wake and cost models can be used in future research to overcome these constraints.

II. Literature review

Several scholars have utilized metaheuristic methods to tackle the problems related to Wind Farm Layout Optimization (WFLO). Application of optimization algorithms for large-scale wind farms was pioneered by Mosetti et al. [10], who sought to maximize energy extraction while lowering installation costs. In a similar vein, Pookpunt and Ongsakul [11] used a genetic algorithm to find the best location for turbines, increasing generation capacity while requiring less land and turbines. Simultaneously, Sood et al. [12] used a random search method similar to Monte Carlo techniques to find the best sites for turbines in small wind farms with different wake characteristics.

Another significant move in the proper improvement process of wind farms and which can enhance the efficiency and effectiveness of wind energy production steps, is Masoudi et al. [13]. An area-rotation layout strategy was created by Shakoor et al. [14] to maximize energy production by optimizing turbine spacing and orientation. A hybrid evolutionary strategy that balances energy production, economic costs, and environmental issues in wind turbine installation was formulate by Bouchekara et al. [15]. Ramli, et al. [16] demonstrated the Multi-Objective Electric Charged Particles improvement process to produce more diverse and robust solutions, which can lead to significant improvements in WF performance. Shin, et al. [17] used the methods of surrogate modeling that enabled to minimize the number of calculations and keep the precision of solutions in large-scale offshore conditions. The authors then concluded that hybrid styles of evolution are especially applicable to offshore WFLO issues because this type of strategy can balance the global exploration and local exploitation in the complex wind conditions. Competitive performance of multi-objective WFLO problems has also been demonstrated by more recent hybrid equilibrium and pattern-search strategies [18].

This research seeks to address the research gap by creating an innovative modified version of Particle Swarm improvement process (PSO) integrated with the Genetic Algorithm (GA), termed PSO-GA, to tackle the WFL-DO challenge.

III. Mathematical Modeling

The optimal operation of a wind farm depends on the strategic placement of turbines to optimize wind resources. Wake interference caused by improper turbine positioning lowers total energy production. In this study, a square area is divided into Nc identical cells (Nc = 100), each measuring 5d × 5d, where "d" stands for the diameter of the turbine rotor. The program finds the best configuration that minimizes cost per energy unit by treating each cell's center as a possible turbine site [18].

PSO-GA hybrid algorithm is evaluated under three distinct wind conditions: (1) constant wind direction and speed, (2) variable wind direction with constant speed, and (3) variable wind direction and speed. In a multi-objective optimization problem, this paradigm aims to maximize energy yield while minimizing cost and wake losses. Extensive simulations demonstrate that PSO-GA outperforms conventional techniques and that the GA component enhances solution refining.

A. Wake Model

Reduced wind velocity downstream of running turbines causes wake losses, which are impacted by intricate nonlinear aerodynamic and environmental phenomena. These consist of blade pitch, yaw angles, airfoil properties, and turbulence intensity. Every turbine creates a wake that grows with distance and interacts with turbines downstream by creating a velocity deficit behind its rotor. Because of its shown dependability in WFLO applications and ease of computing, the Jensen wake model is used here.

As illustrated in Fig. 2, when free-stream wind interacts with the rotor, part of its kinetic energy is extracted for power generation, resulting in a slower airflow downstream. This wake expands due to turbulence, with its radius increasing linearly with distance. Equations (1)–(6) describe the relationship for wake velocity, radius expansion, and partial wake interactions. These expressions enable accurate estimation of wake-induced power losses when multiple turbines operate within proximity.

Equation 1 depicts that if there is no wake loss then downstream velocity of ith turbine is same as free stream wind velocity.

$$v_i = v_o \tag{1}$$

Betz limit is used to measure wind speed for downstream wind turbine as mentioned in equation 2.

$$v = v_o \left[1 - \frac{2a}{1 + \left(\frac{\alpha d}{r}\right)^2} \right] \tag{2}$$

where, r represents the wake radius at distance of d behind the turbine

$$C_T = 4a(1 - a) \tag{3}$$

The wake radius r can be calculated from equation 4.

$$r = \alpha d + r_1 \tag{4}$$

r_1 called the downstream radius of wind turbine and can be measured by equation 5, and α is the wake decay constant and was calculated by equation 6.

$$r_1 = r_r \sqrt{\frac{1 - a}{1 - 2a}} \tag{5}$$

The wind speed that a turbine experiences when its wake is not completely formed is known as the partial wake wind speed. The wind speed in this area, which is nearer the upstream turbine, may

Muhammad Rashid, Syed Mohammad Ali Shah, Abdur Raheem, Saeed Uddin Shaikh, Rabia Shakoor, Zeeshan Ahmad Arfee, Smart Hybrid Metaheuristic Model for Enhanced Wind Energy Production, Journal of Energy, vol. 75 Number 1 (2026), 24–29
https://doi.org/10.37798/2026751739

change. It takes into account the wake model and how the wake only partially covers the rotor area of the downstream turbine, which slows down the wind relative to undisturbed flow.

$$v = v_o \left[1 - \frac{2a}{1 + \left(\frac{\alpha d}{r_1}\right)^2}\right] \frac{A_{T,wake,i}}{A_{T,total,i}} \quad (6)$$

$A_{T,wake,i}$ is the wake-affected area of the i^{th} turbine.

$A_{T,total,i}$ is total area covered by rotor of the i^{th} turbine.

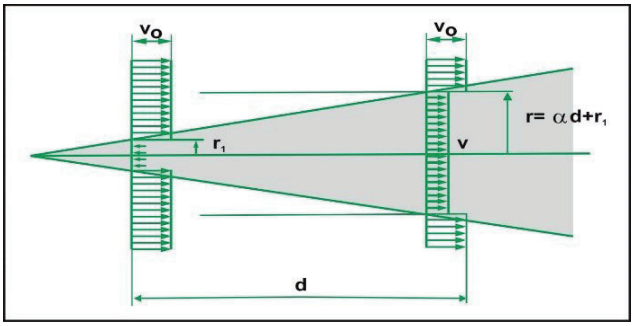

Fig. 2. Single wake effect model.

B. Power Model

The power output of a wind turbine (Pwt) is governed by air density, wind velocity, and rotor radius [19].

Total electrical power (available) by the turbine is measured from equation 7.

$$\text{Electrical Power} = \frac{1}{2}\rho * \pi * r^2 * v^3 * C_p \quad (7)$$

where, ρ is air density, v is the wind velocity, r is the rotor radius & is Power coefficient.

Downstream power taken out from the turbine is measured by the following equation [20].

$$P_{wt} = 0.3V^3 \quad (8)$$

where, v is the downstream wind velocity.

C. Cost Model

The total cost of a wind farm is determined by summing the costs of all installed turbines as expressed in equation (9), where N represents the number of turbines. This cost function is integrated into the optimization objective to ensure a balance between financial feasibility and energy efficiency.

The cost of whole WF is measured by:

$$\text{Cost} = N\left(\frac{2}{3} + \frac{1}{3}e^{-0.00174N^2}\right) \quad (9)$$

where N is the total number of WTs -

D. Objective Function

The primary objective functions of the model is to: (1) Minimize the wake loss (2) Maximize total annual energy production, and (3) Minimize the cost per produced electrical power , as given in equations (10), (11), and (12).

Objective functions of the study are as under.

$$\text{Objective} = \text{Minimize}\left[1 - \frac{2a}{1+\left(\frac{\alpha d}{r}\right)^2}\right] \quad (10)$$

$$\text{Objective} = \text{Maximize}\ \frac{1}{2}\rho * \pi * r^2 * v^3 * C_p \quad (11)$$

$$\text{Objective} = \text{Minimize}\ \frac{\text{Cost}}{\text{Electrical Power}} \quad (12)$$

E. Constraints Modeling

First, all turbines must be located within the predefined wind farm boundary.

$$x_{min} \leq x_i \leq x_{max}$$
$$y_{min} \leq y_i \leq y_{max} \text{ where, } i = 1{:}\,n$$

In this study, the minimum distance is set to eight times the rotor radius (8R), consistent with standard industry guidelines.

IV. Hybrid Optimization Algorithm

This section gives the two metaheuristic algorithms principles—Particle Swarm Optimization (PSO) and Genetic Algorithm (GA)—that form the foundation of the proposed hybrid framework.

A. Particle Swarm Optimization (PSO)

PSO is inspired by the social behavior of birds flocking or fish schooling. Each potential solution is modeled as a 'particle' moving within the search space, influenced by its own best-known position and that of its neighbors [21]. Figure 3 illustrate the PSO process, showing how particles iteratively update positions toward optimal solutions.

B. Genetic Algorithm (GA)

Genetic Algorithm (GA) is a population-based optimization method that draws inspiration from natural selection. To develop superior solutions over successive generations, it uses genetic operators like selection, crossover, and mutation [22]. Figure 4 presents the flowchart of the GA optimization process.

Muhammad Rashid, Syed Mohammad Ali Shah, Abdur Raheem, Saeed Uddin Shaikh, Rabia Shakoor, Zeeshan Ahmad Arfee, Smart Hybrid Metaheuristic Model for Enhanced Wind Energy Production, Journal of Energy, vol. 75 Number 1 (2026), 24–29
https://doi.org/10.37798/2026751739

C. Hybrid PSO-GA Model

The hybridization strategy has two optimization mechanisms. PSO first does global exploration with 100 iterations. They were the inertia weight (w = 0.7), cognitive coefficient (c1 = 2.5) and social coefficient (c2 = 2.5).

Once the convergence has stopped or the PSO iterations are complete, the best 20 percent of the particles in terms of their fitness values are elites. These elite structures are passed on as the first population to the GA module. GA proceeds to use 500 refinement generations with crossover (0.7 rate) and mutation (0.02 rate). Elitism will guarantee that the best solution of PSO prevails. Hybrid transition criterion is activated when the improvement of PSO is less than 10^{-5} on 20 consecutive iterations. Such a design makes PSO do global search and GA improve the local exploitation.

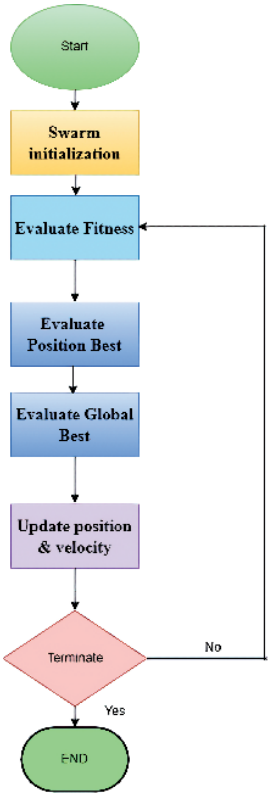

Fig. 3. Flow chart of particle swarm improvement process algorithm.

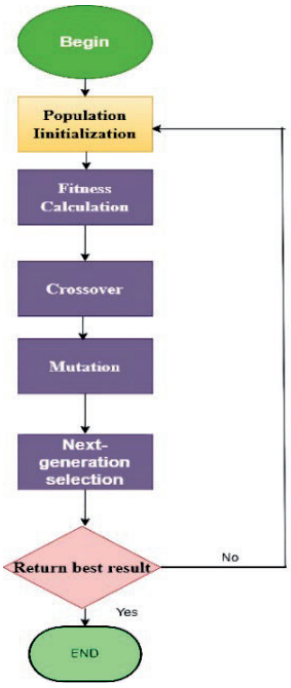

Fig. 4. Flow chart of Genetic algorithm.

V. Results and Discussion

The PSO-GA technique showed a notable increase in the WF's energy yield and cost efficiency through rigorous simulation utilizing the suggested framework.

Three distinct WF designs, each containing a 2 km × 2 km area divided into 100 cells of 200 m × 200 m, were examined in the case studies. With a constant focus on minimizing wake interference while retaining high turbine efficiency and power generation output, the framework was evaluated under various wind speed and wind turbine direction situations.

PSO algorithm explored a broad search space, effectively navigating through multiple local optima to identify promising candidate solutions. The PSO's ability to adjust the particle positions in the search space using its velocity and acceleration coefficients allowed it to investigate various regions of the WF layout space without getting stuck in suboptimal solutions.

GA was used to fine-tune the turbine locations after the PSO had identified a nearly optimal architecture, increasing the energy yield and further minimizing wake disturbance. The genetic operators (crossover and mutation) enabled the algorithm to explore variations in turbine positioning, balancing power yield improvement process with the minimization of wake effects. Through the iterative refinement process, the PSO-GA algorithm outperformed standalone PSO and GA algorithms in terms of the total electrical energy yield.

A. Case I

Figure 5(a) represents the improved layout obtained through the proposed hybrid PSO-GA approach. While, 5(b) reflects the reference layout used for comparison.

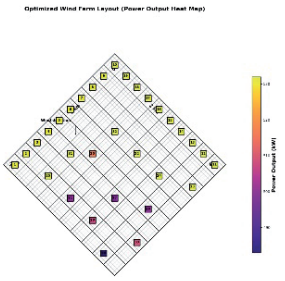

Fig. 5 (a). Layout of wind farm by proposed work.

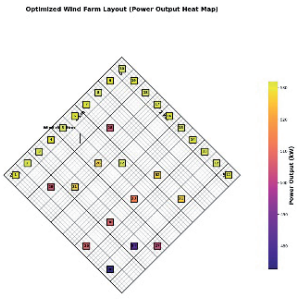

Fig. 5 (b). Layout of wind farm [23].

The optimum configuration produces a maximum power output with 32 turbines working under a uniform inflow wind speed of 12 m/s, as shown in Figures 6(a) and 6(b). An average turbine efficiency of roughly 98.8% and individual turbine efficiencies ranging from 98.8% to 100% show that the algorithm converges on a highly efficient configuration. There is little variance in the effective wind speed distribution between 11.62 and 12.00 m/s throughout the farm.

```
Number of Turbines: 32
Average Turbine Efficiency: 0.988
Efficiency Range: 0.908 - 1.000
Average Effective Wind Speed: 11.95 m/s
Wind Speed Range: 11.62 - 12.00 m/s
```

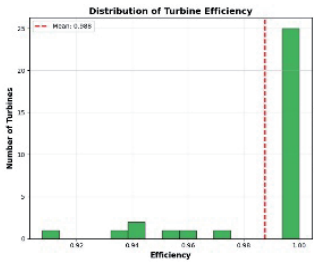

Fig. 6. (a) Optimization outcomes. Fig. 6 (b) Spectra of frequency.

Table I
Performance Analysis Of Case – I

Strategy	Nt	Power Extracted	Wake Loss	AEP (MWh)	Efficiency %
Proposed	32	16389.73	199.06	143574.04	98.8
[23]	32	16326.59	262.2	143020.98	98.42

Table I demonstrates the performance of the proposed layout with previous research. The proposed strategy extracts 16389.73 kW, which is higher than the earlier reported 16326.55 kW. A major difference appears in wake losses: the proposed configuration records 199.06 kW units, in place of 262.21 kW units, indicating that the proposed layout better minimizes wake interactions. Overall, the proposed layout demonstrates superior optimization by

Muhammad Rashid, Syed Mohammad Ali Shah, Abdur Raheem, Saeed Uddin Shaikh, Rabia Shakoor, Zeeshan Ahmad Arfee, Smart Hybrid Metaheuristic Model for Enhanced Wind Energy Production, Journal of Energy, vol. 75 Number 1 (2026), 24–29
https://doi.org/10.37798/2026751739

enhancing power capture and reducing wake-induced losses, outperforming the approach presented in [23].

B. Case 2

Figure 7 (a) represents the improved layout obtained through the proposed hybrid PSO-GA approach. While, 7 (b) reflects the reference layout used for comparison.

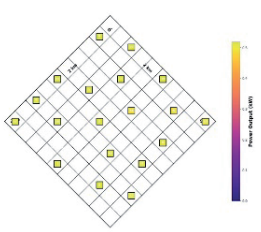

Fig. 7 (a). Layout of wind farm by proposed work.

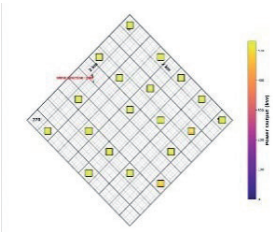

Fig. 7 (b). Layout of wind farm [23].

The optimum configuration produces a maximum power output with 19 turbines working under a uniform inflow wind speed of 12 m/s, as shown in Figures 8(a) and 8(b). With an average turbine efficiency of roughly 99.2% and individual turbine efficiencies ranging from 94.98% to 100%, the algorithm converges on a highly efficient arrangement. There is little fluctuation in the effective wind speed distribution between 11.76 and 12.00 m/s throughout the farm.

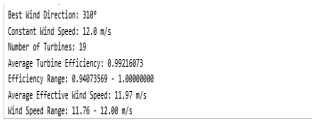

Fig. 8. (a) Optimization results.

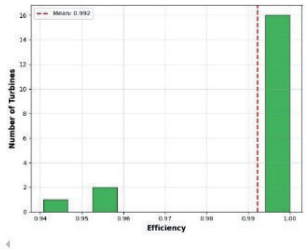

Fig. 8 (b) Distribution of frequency.

The performance of the proposed layout with the previous research is shown in Table II. The suggested method extracts 9770.8 kW, which is marginally more than the 9741.3 kW. Wake loss indicates a significant difference: the suggested configuration records 78.7968 kW units, instead of 108.3 kW units. This suggests that the proposed structure more effectively reduces wake interactions. Overall, by improving power capture and lowering wake-induced losses, the proposed configuration exhibits improved optimization than the technique existing in [23].

Table II
Performance Analysis Of Case - 2

Strategy	Nt	Power Extracted	Wake Loss	AEP	Efficiency %
Proposed	19	9770.8032	78.7968	85592236	99.2
[23]	19	9741.3	108.3	85333788	98.9

In comparison to Asaah et al. (2021), the proposed PSO-GA diminished wake loss by 26.5% in Case 1 and 24.3% in Case 2, concurrently enhancing AEP by roughly 0.2% for each case. In contrast to [23], which depends exclusively on PSO exploration, the hybrid method improves local refinement and convergence dependability.

C. Case 3

Figure 9 illustrates that the chance of wind speed is higher when the wind direction is between 270 and 350. The performance of the suggested layout with the earlier study is shown in Table III. The suggested method extracts 7713.79 kW, which is somewhat more than the 7,690.46 kW. Wake losses indicate a significant difference: the proposed configuration records 62.21 kW units, instead of 85.54 kW units, suggesting that the proposed layout more effectively reduces wake interactions. Overall, by improving power capture and lowering wake-induced losses, the proposed layout do better than the method implemented in [23].

Table III
Performance Analysis Of Case - 3

Strategy	Nt	Power Extracted	Wake Loss	AEP	Efficiency %
Proposed	15	7713.79	62.21	67572800.4	99.2
[23]	15	7,690.46	85.54	67368429.6	98.9

Fig. 9. Wind condition of Case 3.

VI. Conclusion

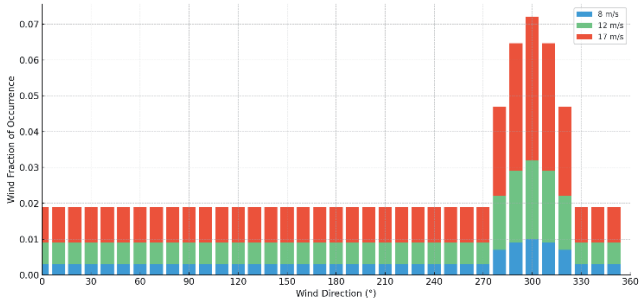

To address the WFLO problem in actual wind conditions, the current study presents a novel hybrid optimization technique that successfully combines Hybrid PSO-GA integrated with the Jensen wake model. Unlike previous research that just used traditional evolutionary algorithms, this approach incorporates a dynamic goal function that takes cost, energy yield, and efficiency by minimizing the wake loss. The paper delineated the optimum WFLOs under the three case studies of wind speed and direction. In order to obtain the maximum possible output power, each WT's position was appropriately selected. In short, the hybrid PSO-GA algorithm provided a very effective method for optimizing wind farm layouts, leading to significant increases in power output and cost effectiveness while preventing severe wake disruption. The algorithm's practical relevance in real-world wind farm design is demonstrated by its robustness across many case studies and its capacity to manage the trade-off between electricity generation and turbine cost. The suggested PSO-GA significantly reduced wake-loss and improved efficiency by up to 0.2% as compared to previous WFLO techniques. The cited 0.2% enhancement pertains to overall agricultural efficiency, whilst the 20–28% decrease specifically relates to wake loss percentage in comparison to the benchmark study. The hybrid framework may be successfully used in actual wind farm planning, as evidenced by the computational cost remaining reasonable. To further increase accuracy, future research might use sophisticated wake models like Gaussian or CFD-based wake formulations.

Muhammad Rashid, Syed Mohammad Ali Shah, Abdur Raheem, Saeed Uddin Shaikh, Rabia Shakoor, Zeeshan Ahmad Arfee, Smart Hybrid Metaheuristic Model for Enhanced Wind Energy Production, Journal of Energy, vol. 75 Number 1 (2026), 24–29
https://doi.org/10.37798/2026751739

References

[1] X. Yu and W. Zhang, "A teaching-learning-based optimization algorithm with reinforcement learning to address wind farm layout optimization problem," *Applied Soft Computing,* vol. 151, 2024, doi: 10.1016/j.asoc.2023.111135.

[2] E. Institute, "Statistical review of world energy," *Technical Report,* 2023.

[3] H. Qin, H. Yang, H. Li, and G. Du, "Highlights of key advances in China's wind turbines technology in 2024," *Frontiers in Energy,* vol. 19, no. 1, pp. 18-27, 2025.

[4] A. McCoy *et al.*, "Offshore wind market report: 2024 edition," National Renewable Energy Laboratory (NREL), Golden, CO (United States), 2024.

[5] A. M. Abdelsalam and M. A. El-Shorbagy, "Optimization of wind turbines siting in a wind farm using genetic algorithm based local search," *Renewable Energy,* vol. 123, pp. 748-755, 2018, doi: 10.1016/j.renene.2018.02.083.

[6] S. Frandsen *et al.*, "Analytical modelling of wind speed deficit in large offshore wind farms," *Wind Energy,* vol. 9, no. 1-2, pp. 39-53, 2006, doi: 10.1002/we.189.

[7] P. Mittal and K. Mitra, "Determining layout of a wind farm with optimal number of turbines: A decomposition based approach," *Journal of cleaner production,* vol. 202, pp. 342-359, 2018.

[8] X. Gao, H. Yang, and L. Lu, "Optimization of wind turbine layout position in a wind farm using a newly-developed two-dimensional wake model," *Applied Energy,* vol. 174, pp. 192-200, 2016.

[9] B. Pérez, R. Mínguez, and R. Guanche, "Offshore wind farm layout optimization using mathematical programming techniques," *Renewable energy,* vol. 53, pp. 389-399, 2013.

[10] G. Mosetti, C. Poloni, and B. Diviacco, "Optimization of wind turbine positioning in large windfarms by means of a genetic algorithm," *Journal of Wind Engineering and Industrial Aerodynamics,* vol. 51, no. 1, pp. 105-116, 1994.

[11] S. Pookpunt and W. Ongsakul, "Optimal placement of wind turbines within wind farm using binary particle swarm optimization with time-varying acceleration coefficients," *Renewable Energy,* vol. 55, pp. 266-276, 2013, doi: 10.1016/j.renene.2012.12.005.

[12] P. Sood, V. Winstead, and P. Steevens, "Optimal placement of wind turbines: A Monte Carlo approach with large historical data set," in *2010 IEEE international conference on electro/information technology*, 2010: IEEE, pp. 1-5.

[13] S. M. Masoudi and M. Baneshi, "Layout optimization of a wind farm considering grids of various resolutions, wake effect, and realistic wind speed and wind direction data: A techno-economic assessment," *Energy,* vol. 244, 2022, doi: 10.1016/j.energy.2022.123188.

[14] R. Shakoor, M. Y. Hassan, A. Raheem, and N. Rasheed, "Wind farm layout optimization using area dimensions and definite point selection techniques," *Renewable energy,* vol. 88, pp. 154-163, 2016.

[15] H. R. Bouchekara, Y. A. Sha'aban, M. S. Shahriar, M. A. Ramli, and A. A. Mas' ud, "Wind Farm Layout Optimization/Expansion with Real Wind Turbines Using a Multi-Objective EA Based on an Enhanced Inverted Generational Distance Metric Combined with the Two-Archive Algorithm 2," *Sustainability,* vol. 15, no. 3, p. 2525, 2023.

[16] M. A. M. Ramli and H. R. E. H. Bouchekara, "Wind Farm Layout Optimization Considering Obstacles Using a Binary Most Valuable Player Algorithm," *IEEE Access,* vol. 8, pp. 131553-131564, 2020, doi: 10.1109/access.2020.3009046.

[17] J. Shin, S. Baek, and Y. Rhee, "Wind farm layout optimization using a metamodel and ea/pso algorithm in korea offshore," *Energies,* vol. 14, no. 1, p. 146, 2020.

[18] R. M. Rizk-Allah and A. E. Hassanien, "A hybrid equilibrium algorithm and pattern search technique for wind farm layout optimization problem," *ISA transactions,* vol. 132, pp. 402-418, 2023.

[19] R. Shakoor, M. Y. Hassan, A. Raheem, and Y.-K. Wu, "Wake effect modeling: A review of wind farm layout optimization using Jensen's model," *Renewable and Sustainable Energy Reviews,* vol. 58, pp. 1048-1059, 2016, doi: 10.1016/j.rser.2015.12.229.

[20] D. Van Der Hoek, J. Frederik, M. Huang, F. Scarano, C. Simao Ferreira, and J.-W. van Wingerden, "Experimental analysis of the effect of dynamic induction control on a wind turbine wake," *Wind Energy Science,* vol. 7, no. 3, pp. 1305-1320, 2022.

[21] Z. A. Arfeen, M. P. Abdullah, M. F. Shehzad, S. Altbawi, M. A. K. Jiskani, and M. A. I. YiRan, "A niche particle swarm optimization-Perks and perspectives," in *2020 IEEE 10th International Conference on System Engineering and Technology (ICSET)*, 2020: IEEE, pp. 102-107.

[22] L. Haldurai, T. Madhubala, and R. Rajalakshmi, "A study on genetic algorithm and its applications," *Int. J. Comput. Sci. Eng,* vol. 4, no. 10, pp. 139-143, 2016.

[23] P. Asaah, L. Hao, and J. Ji, "Optimal Placement of Wind Turbines in Wind Farm Layout Using Particle Swarm Optimization," *Journal of Modern Power Systems and Clean Energy,* vol. 9, no. 2, pp. 367-375, 2021, doi: 10.35833/mpce.2019.000087.

ENERGIJA